

Two-loop electron self-energy in bound-electron g factor: diagrams in momentum-coordinate representation

V. A. Yerokhin,* B. Sikora, Z. Harman, and C. H. Keitel

Max Planck Institute for Nuclear Physics, Saupfercheckweg 1, D 69117 Heidelberg, Germany

The two-loop electron self-energy correction is one of the most problematic QED effects and, for a long time, was the dominant source of uncertainty in the theoretical prediction of the bound-electron g factor in hydrogen-like ions. A major breakthrough was recently achieved in [B. Sikora et al. Phys. Rev. Lett. 134, 123001 (2025)], where this effect was calculated without any expansion in the nuclear binding strength parameter $Z\alpha$ (where Z is the nuclear charge number and α is the fine-structure constant). In this paper, we describe our calculations of one of the most difficult parts of the two-loop self-energy, represented by Feynman diagrams that are treated in the mixed momentum-coordinate representation.

I. INTRODUCTION

The g factor of the bound electron in hydrogen-like ions has been measured with exceptional accuracy of up to 11 significant figures [1–7], thus challenging theorists to match this precision in the bound-state QED calculations. After many-years efforts and dedicated calculations, theory has been able to reach the 10^{-11} accuracy level for light hydrogen-like ions, such as carbon and oxygen [8–13]. For higher- Z ions, however, theory suffered from a dramatic loss of precision, mostly from uncalculated two-loop QED contributions. There have been significant efforts invested in calculations of two-loop QED effects, both within expansion in the parameter $Z\alpha$ [14–16] and without [17, 18] in last years. They resulted in a better theoretical understanding of the g factors in the low- Z region but did not significantly improved theoretical accuracy in the high- Z region. In particular, for the heaviest measured element, tin ($Z = 50$), a theoretical accuracy of about 10^{-7} was recently reported in Ref. [7], substantially inferior to the 10^{-10} experimental accuracy achieved in the same work. The main factor limiting the theoretical accuracy was the two-loop self-energy correction. Because its $Z\alpha$ expansion converges slowly, any substantial progress for the g factor of tin (as well as heavier elements) could be achieved only through a calculation nonperturbative in the parameter $Z\alpha$.

The two-loop self-energy correction has been calculated without expansion in $Z\alpha$ for the *Lamb shift* in a series of investigations [19–25]. Carrying out analogous calculations for the bound-electron g factor is even more challenging. The corresponding project was initiated about a decade ago. Several individual contributions have been computed [26, 27] but two of the most difficult parts of the two-loop self-energy correction, the so-called M and P terms, remained uncalculated. A breakthrough was achieved in our recent Letter [28], where the complete calculation of the two-loop self-energy correction to the g -factor was reported for the hydrogen-like tin ion.

This calculation enhanced theoretical accuracy by an order of magnitude and significantly improved agreement of the theoretical prediction of the tin g factor with the experimental value [7].

The goal of the present investigation is to present our method developed for the P -term part of the two-loop self-energy correction and perform numerical calculations for hydrogen-like ions with $Z \geq 50$. The corresponding Feynman diagrams contain both the Dirac-Coulomb propagators and ultraviolet-diverging free-electron subgraphs. For this reason, their calculation needs to be performed in the mixed momentum-coordinate representation. Such contributions are characteristic for non-factorizable two-loop QED effects and were encountered for the first time in the Lamb-shift calculations of the two-loop self-energy. In early studies [29, 30], they were computed by using the B -spline finite-basis representation of the Dirac-Coulomb spectrum and the subsequent numerical Fourier transformation. Later on, a different technique was developed [31] which used the analytical representation of the Dirac-Coulomb Green function in terms of Whittaker functions. This technique allowed to improve the numerical precision and obtain accurate results for the two-loop Lamb shift [24, 25]. In the present work, we extend the technique developed for the Lamb shift to the case of the bound-electron g factor.

The relativistic units ($\hbar = c = m = 1$) and the Heaviside charge units ($\alpha = e^2/4\pi$, $e < 0$) are used throughout this paper. We use roman style (p) for four vectors, arrows \vec{p} for three vectors, and italic style (p) for scalars. Four vectors have the form $p = (p_0, \vec{p})$. The Feynman gauge will be used in this work.

II. BASIC FORMULATION

The g factor of an atomic system is observed as a shift of atomic energy levels due to the interaction with a weak external magnetic field (the linear Zeeman effect). The interaction potential is

$$V_{\text{Zee}}(\vec{r}) = -e \vec{\alpha} \cdot \vec{A}(\vec{r}), \quad (1)$$

* Corresponding author: vladimir.yerokhin@mpi-hd.mpg.de

where $\vec{A}(\vec{r}) = (1/2)[\vec{B} \times \vec{r}]$ is the vector potential, $\vec{\alpha}$ is the vector of Dirac matrices and e is the electron charge. In practical calculations, it is convenient to introduce the effective g -factor potential V_g [32],

$$V_g(\vec{r}) = \frac{1}{\mu_a} (\vec{r} \times \vec{\alpha})_z, \quad (2)$$

where μ_a denotes the angular momentum projection of the reference state and the subscript z indicates the projection on the z axis. The effective potential V_g does not depend on the magnetic field and its expectation value yields directly the g -factor value. So, for the $1s$ reference state and point nucleus, one obtains the well-known Dirac value of a bound-electron g factor,

$$g_D = \langle a | V_g | a \rangle = \frac{2}{3} \left(1 + 2\sqrt{1 - (Z\alpha)^2} \right). \quad (3)$$

The two-loop self-energy (SESE) correction to the g factor of a bound electron is graphically represented in Fig. 1. Feynman diagrams in the first line are known as the loop-after-loop (LAL) diagrams. They can be factorized in terms of the self-energy contributions of lower orders. Their analysis and calculation was reported in our previous investigations [26, 27]. In the present work we will be concerned with the nested and overlapping diagrams shown in the second and the third lines of Fig. 1, respectively.

The nested (N) and overlapping (O) diagrams in Fig. 1 are of two types: (i) with the magnetic interaction attached to the external wave function [diagrams (d) and (g)] and (ii) with the magnetic interaction attached to the electron propagators [diagrams (e), (f), (h) and (i)]. Contributions of diagrams of first type are divided into the irreducible (with $n \neq a$) and the reducible (with $n = a$) parts, where n denotes an intermediate electron state in the propagator next to the magnetic interaction and a is the reference state. The irreducible contributions will be referred to as the *perturbed-orbital* (W) terms. They have the following structure

$$E_{hW} = \langle a | \Sigma_h | \delta a \rangle + \langle \delta a | \Sigma_h | a \rangle, \quad (4)$$

where $h = (N, O)$ and the operators $\Sigma_h = \Sigma_N$ and Σ_O are the nested and overlapping irreducible operators, respectively, which appeared in two-loop calculations for the Lamb shift. Furthermore, $|\delta a\rangle$ is the first-order perturbation of the reference-state wave function $|a\rangle$ by V_g ,

$$|\delta a\rangle = \sum_{n \neq a} \frac{|n\rangle \langle n| V_g |a\rangle}{\varepsilon_a - \varepsilon_n}. \quad (5)$$

The reducible contributions will be referred to as the *derivative* (D) terms. They have the following structure

$$E_{hD} = \langle a | V_g | a \rangle \langle a | \frac{\partial \Sigma_h(\varepsilon)}{\partial \varepsilon} | a \rangle \Big|_{\varepsilon=\varepsilon_a}. \quad (6)$$

Contributions of diagrams with the magnetic interaction attached to the electron propagators are referred to

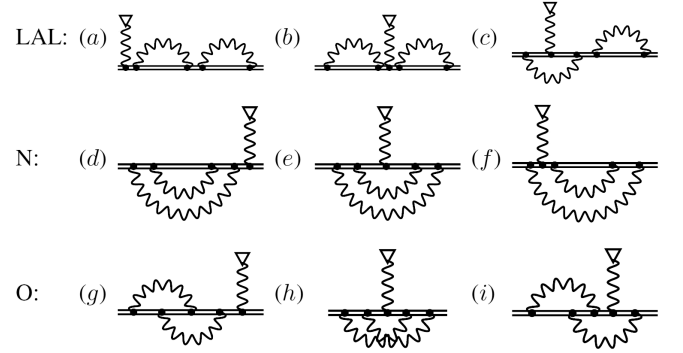


FIG. 1: Feynman diagrams representing the two-loop electron self-energy (SESE) correction for the bound-electron g factor: (a)-(c) loop-after-loop (LAL), (d)-(f) nested (N), (g)-(i) overlapping (O) diagrams. The double line denotes the electron in the presence of the binding nuclear field; the wavy line indicates the exchange of a virtual photon; the wavy line terminated by a triangle denotes the interaction with the external magnetic field.

as the *vertex* (V) corrections. They are irreducible and have the following structure

$$E_{hV} = \langle a | \Lambda_h | a \rangle, \quad (7)$$

where $h = (NL, NS, OL, OS)$. Λ_{NL} , Λ_{NS} , Λ_{OL} , and Λ_{OS} are the nested (N) and overlapping (O) ladder (L) and side (S) operators depicted in Fig. 1(e), (f), (h), and (i), respectively.

Formal expressions for the SESE correction discussed so far suffer from ultraviolet (UV) and infrared (IR) divergencies that need to be eliminated before any actual numerical calculations can be performed. First we discuss the renormalization and elimination of UV divergences. Following the approach developed for the Lamb shift [19, 21, 29, 33], we base our renormalization procedure on separation of one or two first terms of expansion of the Dirac-Coulomb propagator G in the number of interactions with the binding Coulomb field $V_C(r) = -Z\alpha/r$. Specifically,

$$G(\varepsilon, \vec{x}_1, \vec{x}_2) = G^{(0)}(\varepsilon, \vec{x}_1, \vec{x}_2) + G^{(1)}(\varepsilon, \vec{x}_1, \vec{x}_2) + G^{(2)}(\varepsilon, \vec{x}_1, \vec{x}_2) + \dots, \quad (8)$$

where the index k in $G^{(k)}$ denotes the number of interactions with V_C . The Dirac-Coulomb propagator is defined as

$$G(\varepsilon, \vec{x}_1, \vec{x}_2) = \sum_n \frac{\psi_n(\vec{x}_1) \psi_n^\dagger(\vec{x}_2)}{\varepsilon - \varepsilon_n}, \quad (9)$$

where $\psi_n(\vec{x})$ are solutions of the Dirac equation with the Coulomb potential V_C , ε_n are the corresponding energies, and the sum over n implies the summation over the full Dirac spectrum (i.e., summation over the principal quantum number of the bound states, integration

over the continuum states, summations over the angular-momentum quantum number κ_n and the angular momentum projections μ_n). Furthermore, $G^{(0)}$ is the free-electron propagator, which is the limiting value of G at $Z \rightarrow 0$. The free-electron propagator is known both in coordinate as well as momentum space. In momentum representation, it is just

$$G(\varepsilon, \vec{p}) = \frac{1}{\not{p} - m} \gamma^0, \quad (10)$$

where $\not{p} = \gamma_\mu p^\mu$ and $\mathbf{p} = (\varepsilon, \vec{p})$. The one-potential Green function $G^{(1)}$ contains one interaction with the binding nuclear potential and is given by

$$G^{(1)}(\varepsilon, \vec{x}_1, \vec{x}_2) = \int d\vec{x}_3 G^{(0)}(\varepsilon, \vec{x}_1, \vec{x}_3) V_C(x_3) G^{(0)}(\varepsilon, \vec{x}_3, \vec{x}_2). \quad (11)$$

The renormalization procedure at the two-loop level was developed for the Lamb shift in Refs. [19, 21, 29, 33] and generalized for the g -factor in Refs. [26, 27]. The resulting diagrams to be computed are divided into three classes: (i) those calculated in coordinate space (M -term), (ii) those calculated in the mixed momentum-coordinate representation (P -term) and (iii) those computed in momentum space (F -term). So, each of the nested and overlapping contributions is represented as a sum of the M -, P -, and F -term parts,

$$E_i = E_i^M + E_i^P + E_i^F. \quad (12)$$

In the present work, we will concentrate on the P -term contributions. We define the P term to be both UV and IR finite, so it can be computed separately from the remaining parts of the SESE correction.

The main complication of the two-loop diagrams as compared to the one-loop case is the presence of the overlapping UV divergences. E.g., the nested diagrams shown in Fig. 1(d)-(f) can UV diverge due to the inner self-energy loop or due to the outer self-energy loop, or both. This means that if we renormalize the inner loop, the overall diagram will be still divergent due to the outer loop. The distinct feature of the P -term contributions is that they contain an one-loop UV-divergent subgraph (the free-electron self-energy or the free-electron vertex), whereas the UV divergency of the overall diagram is cancelled by suitably chosen subtractions. The one-loop subgraph is renormalized and calculated in momentum space. The outer diagram contains Dirac-Coulomb propagators which are known in coordinate space. As a compromise, we perform our computations in the mixed momentum-coordinate representations, with the renormalized one-loop subgraph computed in momentum space, whereas the outer diagram is calculated in coordinate space. Each of the P -term contributions contains one unbounded partial-wave expansion, which originates from Dirac-Coulomb propagators.

III. PERTURBED-ORBITAL CONTRIBUTIONS

The perturbed-orbital P -term contributions are diagrammatically represented in Fig. 2. They are related to the corresponding contributions to the Lamb shift that appeared in our previous investigations [23, 31]. Their expressions can be obtained by perturbing the external reference-state wave functions in the Lamb-shift expressions by the magnetic potential, $\psi_a \rightarrow \psi_{\delta a}$, where $\psi_{\delta a}$ is given by Eq. (5).

A. E_{NW1}^P

This correction can be obtained from the $N1$ P -term contribution to the Lamb shift [see Eq. (113) of Ref. [30]] by perturbing the external wave functions, $\psi_a \rightarrow \psi_{\delta a}$ (the first line of Fig. 2). The result is

$$\begin{aligned} E_{\text{NW1}}^P = & 2i\alpha \int_{C_F} d\omega \int \frac{d\vec{p}}{(2\pi)^3} \int d\vec{x}_1 d\vec{x}_2 D(\omega, x_{12}) \psi_a^\dagger(\vec{x}_1) \alpha_\mu \left\{ G(E, \vec{x}_1, \vec{p}) \gamma^0 \Sigma_R^{(0)}(E, \vec{p}) G(E, \vec{p}, \vec{x}_2) \right. \\ & - G^{(0)}(E, \vec{x}_1, \vec{p}) \gamma^0 \Sigma_R^{(0)}(E, \vec{p}) G^{(0)}(E, \vec{p}, \vec{x}_2) - G^{(1)}(E, \vec{x}_1, \vec{p}) \gamma^0 \Sigma_R^{(0)}(E, \vec{p}) G^{(0)}(E, \vec{p}, \vec{x}_2) \\ & \left. - G^{(0)}(E, \vec{x}_1, \vec{p}) \gamma^0 \Sigma_R^{(0)}(E, \vec{p}) G^{(1)}(E, \vec{p}, \vec{x}_2) \right\} \alpha^\mu \psi_{\delta a}(\vec{x}_2) + (\psi_a \leftrightarrow \psi_{\delta a}), \end{aligned} \quad (13)$$

where $E \equiv \varepsilon_a - \omega$, $D(\omega, x_{12})$ is the scalar part of the photon propagator in the Feynman gauge,

$$D(\omega, x_{12}) = \frac{\exp(i\sqrt{\omega^2 + i0} x_{12})}{4\pi x_{12}}, \quad (14)$$

where the branch of the square root is fixed by the condition $\text{Im}(\sqrt{\omega^2 + i0}) > 0$, and $x_{12} = |\vec{x}_1 - \vec{x}_2|$. Furthermore, $\Sigma_R^{(0)}$ is the renormalized free-electron self-energy operator in $D = 4$ dimensions, see Eq. (241) of Ref. [30], C_F is the standard Feynman integration contour, and $\psi_{\delta a}$ is the perturbed reference-state wave function (5). The Dirac-Coulomb Green function in the mixed coordinate-momentum representation is defined as a Fourier transform of the

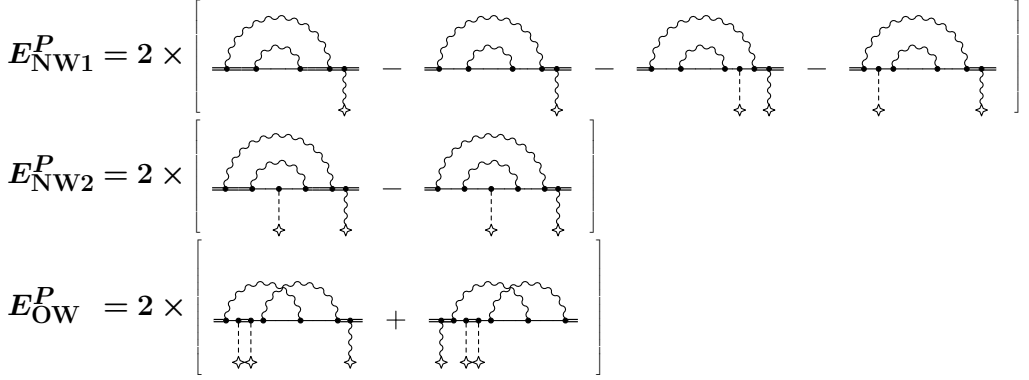


FIG. 2: Diagrammatic representation of the perturbed-orbital P -term contributions. A double line denotes the bound electron propagator, the single line denotes the free electron propagator, the wave line denotes the photon propagator, the dashed line terminated by a stylized cross denotes the interaction with the Coulomb nuclear field, the wave line terminated by the stylized cross denotes the interaction with the external magnetic field.

coordinate-space Dirac-Coulomb Green function over one of the radial variables [30],

$$G(\varepsilon, \vec{x}_1, \vec{p}) = \int d\vec{x}_2 e^{i\vec{p} \cdot \vec{x}_2} G(\varepsilon, \vec{x}_1, \vec{x}_2), \quad G(\varepsilon, \vec{p}, \vec{x}_2) = \int d\vec{x}_1 e^{-i\vec{p} \cdot \vec{x}_1} G(\varepsilon, \vec{x}_1, \vec{x}_2). \quad (15)$$

For convenience of the numerical evaluation, the integrand in curly brackets in Eq. (13) was transformed as [31]

$$\begin{aligned} \{ \dots \} &= G_V(E, \vec{x}_1, \vec{p}) \frac{1}{\not{p} - m} \Sigma_R^{(0)}(E, \vec{p}) \frac{1}{\not{p} - m} G_V(E, \vec{p}, \vec{x}_2) \\ &\quad + 2 \left[G_V(E, \vec{x}_1, \vec{p}) - G_V^{(0)}(E, \vec{x}_1, \vec{p}) \right] \frac{1}{\not{p} - m} \Sigma_R^{(0)}(E, \vec{p}) G^{(0)}(E, \vec{p}, \vec{x}_2), \end{aligned} \quad (16)$$

where $\not{p} = \gamma^0 E - \vec{\gamma} \cdot \vec{p}$ and G_V denotes the Fourier transform of the product of the Green function and the Coulomb potential [31],

$$G_V(\varepsilon, \vec{x}_1, \vec{p}) = \int d\vec{x}_2 e^{i\vec{p} \cdot \vec{x}_2} G(\varepsilon, \vec{x}_1, \vec{x}_2) V_C(x_2), \quad G_V(\varepsilon, \vec{p}, \vec{x}_2) = \int d\vec{x}_1 e^{-i\vec{p} \cdot \vec{x}_1} V_C(x_1) G(\varepsilon, \vec{x}_1, \vec{x}_2). \quad (17)$$

The last term in Eq. (16) contains a combinatorial factor of 2 that accounts for the contributions of two equivalent diagrams. Note that these two diagrams become equivalent only after the symmetrization $\psi_a \leftrightarrow \psi_{\delta a}$. The idea behind the transformation (16) is that it separates out the additional free-electron propagator(s), which decrease as $\sim 1/p$ for large momenta. This separation simplifies the numerical integration over p since it makes the integrand to behave better for large p . It should be noted that, contrary to the Lamb-shift case, $E_{\text{NW}1}^P$ does not contain IR divergences. The reason is that the reference-state contribution in the IR (i.e., small- ω) region is regularized by the orthogonality of $\psi_{\delta a}$ and ψ_a , $\langle \delta a | a \rangle = 0$. For this reason, there are no infrared subtractions in $E_{\text{NW}1}^P$. We compute $E_{\text{NW}1}^P$ by generalizing the code developed for the Lamb shift and described in our previous publications [23, 31].

B. $E_{\text{NW}2}^P$

This correction can be obtained from the N2 P -term contribution to the Lamb shift [see Eq. (117) of Ref. [30]] by perturbing the external wave functions, $\psi_a \rightarrow \psi_{\delta a}$ (the second line of Fig. 2). The result is

$$\begin{aligned} E_{\text{NW}2}^P &= 2i\alpha \int_{C_F} d\omega \int \frac{d\vec{p}_1}{(2\pi)^3} \frac{d\vec{p}_2}{(2\pi)^3} \int d\vec{x}_1 d\vec{x}_2 D(\omega, x_{12}) V_C(\vec{q}) \psi_a^\dagger(\vec{x}_1) \alpha_\mu \left\{ G(E, \vec{x}_1, \vec{p}_1) \gamma^0 \Gamma(E, \vec{p}_1; E, \vec{p}_2) G(E, \vec{p}_2, \vec{x}_2) \right. \\ &\quad \left. - G^{(0)}(E, \vec{x}_1, \vec{p}_1) \gamma^0 \Gamma(E, \vec{p}_1; E, \vec{p}_2) G^{(0)}(E, \vec{p}_2, \vec{x}_2) \right\} \alpha^\mu \psi_{\delta a}(\vec{x}_2) + (\psi_a \leftrightarrow \psi_{\delta a}), \end{aligned} \quad (18)$$

where $\Gamma(E, \vec{p}_1; E, \vec{p}_2)$ is the time component of the renormalized one-loop vertex operator in $D = 4$ dimensions, $\Gamma \equiv \Gamma_R^0$ (for brevity we will suppress the indices here), see Eq. (257) of Ref. [30] and Appendix B of Ref. [34]. For

convenience of the numerical evaluation, the integrand in curly brackets in Eq. (18) is transformed as [31]

$$\begin{aligned} \{ \dots \} &= G_V(E, \vec{x}_1, \vec{p}_1) \frac{1}{\not{p}_1 - m} \Gamma(E, \vec{p}_1; E, \vec{p}_2) \frac{1}{\not{p}_2 - m} G_V(E, \vec{p}_2, \vec{x}_2) \\ &\quad + 2 G_V(E, \vec{x}_1, \vec{p}_1) \frac{1}{\not{p}_1 - m} \Gamma(E, \vec{p}_1; E, \vec{p}_2) G^{(0)}(E, \vec{p}_2, \vec{x}_2), \end{aligned} \quad (19)$$

where $\not{p}_{1,2} = \gamma^0 E - \vec{\gamma} \cdot \vec{p}_{1,2}$ and the combinatorial factor of 2 accounts for two equivalent diagrams.

Equation (18) contains two integrations over momenta, \vec{p}_1 and \vec{p}_2 . Its numerical evaluation is complicated by the presence of the (integrable) Coulomb singularity at $\vec{p}_1 = \vec{p}_2$ coming through the Coulomb potential $V_C(\vec{q})$. It is advantageous to separate out the diagonal in momentum contribution of the vertex operator and evaluate it separately. Therefore, we split the vertex operator into the diagonal and the nondiagonal (in momentum) parts,

$$\Gamma(E, \vec{p}_1; E, \vec{p}_2) = \Gamma_{\text{dia}}(E, \vec{p}_1) + \Gamma_{\text{ndia}}(E, \vec{p}_1; E, \vec{p}_2) \equiv \Gamma(E, \vec{p}_1; E, \vec{p}_1) + \left[\Gamma(E, \vec{p}_1; E, \vec{p}_2) - \Gamma(E, \vec{p}_1; E, \vec{p}_1) \right]. \quad (20)$$

In the diagonal part, the integration over one momentum (and the Coulomb singularity) is carried out analytically by using the identity

$$\int \frac{d\vec{p}_2}{(2\pi)^3} V_C(\vec{p}_1 - \vec{p}_2) G(\vec{p}_2, \vec{x}_2) = G_V(\vec{p}_1, \vec{x}_2). \quad (21)$$

Eq. (18) is very similar to the corresponding part of the P -term for the Lamb shift. An important difference is that $E_{\text{NW}2}^P$, similarly to $E_{\text{NW}1}^P$ and contrary to the Lamb-shift case, does not contain IR divergences, because of the orthogonality of ψ_a and $\psi_{\delta a}$. We compute this contribution by generalizing the code developed for the Lamb shift and described in our previous studies [23, 31].

C. E_{OW}^P

This correction can be obtained from the overlapping P -term contribution to the Lamb shift [see Eq. (120) of Ref. [30]] by perturbing the external wave functions, $\psi_a \rightarrow \psi_{\delta a}$ (see the third line of Fig. 2). The result is

$$\begin{aligned} E_{\text{OW}}^P &= -4i\alpha \int_{C_F} d\omega \int \frac{d\vec{p}_1}{(2\pi)^3} \frac{d\vec{p}_2}{(2\pi)^3} \int d\vec{z} \frac{e^{-i\vec{q} \cdot \vec{z}}}{\omega^2 - \vec{q}^2 + i0} \psi_a^\dagger(\vec{x}_1) \alpha_\mu \\ &\quad \times G^{(2+)}(E, \vec{x}_1, \vec{p}_1) \gamma^0 \Gamma_R^\mu(E, \vec{p}_1; \varepsilon_a, \vec{p}_2) \psi_{\delta a}(\vec{p}_2) + (\psi_a \leftrightarrow \psi_{\delta a}), \end{aligned} \quad (22)$$

where $G^{(2+)} = G - G^{(0)} - G^{(1)}$ is the electron propagator with two or more interactions with the binding potential, and Γ_R^μ is the renormalized free-electron vertex operator in $D = 4$ dimensions, see Eq. (257) of Ref. [30] and Appendix B of Ref. [34]. The computation of this contribution was performed as described in Ref. [23], after transforming the integrand as follows

$$G^{(2+)}(E, \vec{x}_1, \vec{p}_1) \gamma^0 \Gamma_R^\mu(E, \vec{p}_1; \varepsilon_a, \vec{p}_2) = \left[G_V(E, \vec{x}_1, \vec{p}_1) - G_V^{(0)}(E, \vec{x}_1, \vec{p}_1) \right] \frac{1}{\not{p}_1 - m} \Gamma_R^\mu(E, \vec{p}_1; \varepsilon_a, \vec{p}_2). \quad (23)$$

IV. DERIVATIVE CONTRIBUTIONS

The derivative P -term contributions are shown in Fig. 3. They are related to the P -term contributions for the Lamb shift. As compared to their Lamb-shift counterparts, they contain a derivative of one of the electron propagators over the energy argument. The derivative is equivalent to the insertion of a scalar vertex into the corresponding Feynman diagram,

$$\frac{\partial}{\partial \varepsilon} G(\varepsilon, \vec{x}_1, \vec{x}_2) = - \int d\vec{x}_3 G(\varepsilon, \vec{x}_1, \vec{x}_3) G(\varepsilon, \vec{x}_3, \vec{x}_2). \quad (24)$$

The additional vertex in the diagrams not only makes the numerical evaluation more difficult than in the Lamb-shift case, but also enhances the degree of IR divergences.

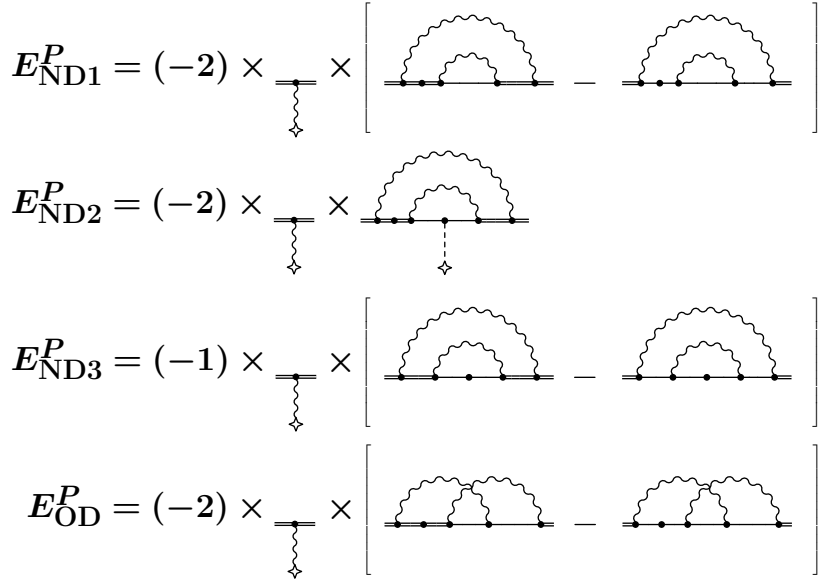


FIG. 3: Diagrammatic representation of the derivative P -term contributions.

A. E_{ND1}^P

The first nested derivative contribution is induced by the first line of Fig. 3. Its expression is given by

$$E_{ND1}^P = (-2) \langle V_g \rangle 2i\alpha \int_{C_F} d\omega \int \frac{d\vec{p}}{(2\pi)^3} \int d\vec{x}_1 d\vec{x}_2 d\vec{x}_3 D(\omega, x_{12}) \psi_a^\dagger(\vec{x}_1) \alpha_\mu \\ \times \left[G(E, \vec{x}_1, \vec{x}_3) G(E, \vec{x}_3, \vec{p}) \gamma^0 \Sigma_R^{(0)}(E, \vec{p}) G(E, \vec{p}, \vec{x}_2) \right. \\ \left. - G^{(0)}(E, \vec{x}_1, \vec{x}_3) G^{(0)}(E, \vec{x}_3, \vec{p}) \gamma^0 \Sigma_R^{(0)}(E, \vec{p}) G^{(0)}(E, \vec{p}, \vec{x}_2) \right] \alpha^\mu \psi_a(\vec{x}_2), \quad (25)$$

where $\langle V_g \rangle$ is the expectation value of the effective g -factor operator given by Eq. (3) and $\Sigma_R^{(0)}(E, \vec{p})$ is the renormalized free-electron self-energy operator. In order to separate the infrared divergences present in the above expression, we subtract and re-add the following terms in the expression in the brackets,

$$[\dots] = [\dots \mp G^{(a)}(E, \vec{x}_1, \vec{x}_3) G(E, \vec{x}_3, \vec{p}) \gamma^0 \left(\Sigma_R^{(0)}(\varepsilon_a, \vec{p}) - \omega \Sigma_R^{(0)'}(\varepsilon_a, \vec{p}) \right) G^{(a)}(E, \vec{p}, \vec{x}_2)], \quad (26)$$

where $\Sigma_R^{(0)'}(\varepsilon_a, \vec{p}) = d/(d\varepsilon) \Sigma_R^{(0)}(\varepsilon, \vec{p})|_{\varepsilon=\varepsilon_a}$ and $G^{(a)}$ is the reference-state part of the Dirac-Coulomb propagator defined as

$$G^{(a)}(\varepsilon, \vec{x}_1, \vec{x}_2) = \sum_{\mu_{a'}} \frac{\psi_{a'}(\vec{x}_1) \psi_{a'}^\dagger(\vec{x}_2)}{\varepsilon - \varepsilon_a}, \quad (27)$$

where a' denotes the electron state that differs from the reference-state a only by the angular-momentum projection $\mu_{a'}$. The sign \mp in Eq. (26) means that we subtract the infrared-divergent part and then re-add it and evaluate separately. This leads to a separation of E_{ND1}^P into the regular (R) and two infrared-divergent (IR', IR) contributions,

$$E_{ND1}^P = E_{ND1}^P(R) + E_{ND1}^P(IR') + E_{ND1}^P(IR). \quad (28)$$

The infrared IR and IR' contributions are regularized by introducing a fictitious finite photon mass μ ; the ω integration in them is evaluated analytically. After IR-divergent contributions are added together, the μ divergence disappears and the limit $\mu \rightarrow 0$ can be taken. Here and in what follows we will denote the linearly-divergent ($\sim 1/\mu$) infrared contribution as IR', and the logarithmically-divergent ($\sim \ln \mu$) infrared contribution as IR. Noting that in Eq. (26) the free-electron operators do not depend on ω , we factorize out the infrared terms and obtain

$$E_{ND1}^P(IR') = (-2) \langle V_g \rangle \langle \gamma^0 \Sigma_R^{(0)}(\varepsilon_a) \rangle J_3, \quad E_{ND1}^P(IR) = (-2) \langle V_g \rangle \langle \gamma^0 \Sigma_R^{(0)'}(\varepsilon_a) \rangle J_2. \quad (29)$$

Here, J_2 and J_3 are basic IR-divergent integrals defined as (see Appendix B of Ref. [35])

$$J_\alpha = \sum_{\mu_{a'}} \frac{i}{2\pi} \int_{C_F} d\omega \frac{\langle aa' | I_\mu(\omega) | a' a \rangle}{(-\omega + i0)^\alpha}, \quad (30)$$

where $I_\mu(\omega)$ is the electron-electron interaction operator with a finite photon mass μ ,

$$I_\mu(\omega, x_{12}) = \alpha \alpha_\sigma \alpha^\sigma \frac{e^{i\sqrt{\omega^2 - \mu^2 + i0} x_{12}}}{x_{12}}. \quad (31)$$

The IR divergent integrals are evaluated as [35]

$$J_2 = \frac{\alpha}{\pi} \left[\ln \frac{\mu}{2} + \gamma + \sum_{\mu_{a'}} \langle aa' | \alpha_\sigma \alpha^\sigma \ln x_{12} | a' a \rangle \right], \quad J_3 = \frac{\alpha}{4} \left[\frac{1}{\mu} - \sum_{\mu_{a'}} \langle aa' | \alpha_\sigma \alpha^\sigma x_{12} | a' a \rangle \right]. \quad (32)$$

For the numerical evaluation it is convenient to transform the integrand of Eq. (25) to a form that does not involve subtraction of the free-electron contribution. We thus write the integrand as

$$\begin{aligned} \int d\vec{x}_3 \left[G(E, \vec{x}_1, \vec{x}_3) G(E, \vec{x}_3, \vec{p}) \gamma^0 \Sigma_R^{(0)}(E, \vec{p}) G(E, \vec{p}, \vec{x}_2) - G^{(0)}(E, \vec{x}_1, \vec{x}_3) G^{(0)}(E, \vec{x}_3, \vec{p}) \gamma^0 \Sigma_R^{(0)}(E, \vec{p}) G^{(0)}(E, \vec{p}, \vec{x}_2) \right] = \\ = G_V(E, \vec{x}_1, \vec{p}) \frac{1}{\not{p} - m} \gamma^0 \frac{1}{\not{p} - m} \Sigma_R^{(0)}(E, \vec{p}) G^{(0)}(E, \vec{p}, \vec{x}_2) \\ + G(E, \vec{x}_1, \vec{p}) \frac{1}{\not{p} - m} \Sigma_R^{(0)}(E, \vec{p}) \frac{1}{\not{p} - m} \gamma^0 G_V(E, \vec{p}, \vec{x}_2) \\ + \int d\vec{x}_3 G(E, \vec{x}_1, \vec{x}_3) G_V(E, \vec{x}_3, \vec{p}) \frac{1}{\not{p} - m} \Sigma_R^{(0)}(E, \vec{p}) G(E, \vec{p}, \vec{x}_2), \end{aligned} \quad (33)$$

with $\not{p} = \gamma^0 E - \vec{\gamma} \cdot \vec{p}$. An advantage of the representation (33) is that each of the three terms in the right-hand-side contains at least one Coulomb interaction explicitly. A useful check for the numerical procedure for E_{ND1}^P can be obtained by making the replacement $\gamma^0 \Sigma_R^{(0)}(\varepsilon, \vec{p}) \rightarrow 1$, after which the contribution can be computed entirely in coordinate representation. Specifically, after this replacement the regular part of E_{ND1}^P becomes

$$\begin{aligned} E_{\text{ND1}}^P(\mathbf{R}) \rightarrow (-2) \langle V_g \rangle 2i\alpha \int_{C_F} d\omega \int d\vec{x}_1 d\vec{x}_2 D(\omega, x_{12}) \psi_a^\dagger(\vec{x}_1) \alpha_\mu \\ \times \frac{1}{2} \frac{\partial^2}{(\partial E)^2} \left[G(E, \vec{x}_1, \vec{x}_2) - G^{(0)}(E, \vec{x}_1, \vec{x}_2) - G^{(a)}(E, \vec{x}_1, \vec{x}_2) \right] \alpha^\mu \psi_a(\vec{x}_2), \end{aligned} \quad (34)$$

which can be computed in a straightforward manner in coordinate space.

B. E_{ND2}^P

The second nested derivative contribution is induced by the second line of Fig. 3 and is expressed as

$$\begin{aligned} E_{\text{ND2}}^P = & (-2) \langle V_g \rangle 2i\alpha \int_{C_F} d\omega \int \frac{d\vec{p}_1}{(2\pi)^3} \frac{d\vec{p}_2}{(2\pi)^3} \int d\vec{x}_1 d\vec{x}_2 d\vec{x}_3 D(\omega, x_{12}) V_C(q) \psi_a^\dagger(\vec{x}_1) \alpha_\mu \\ & \times \left[G(E, \vec{x}_1, \vec{x}_3) G(E, \vec{x}_3, \vec{p}_1) \gamma^0 \Gamma(E, \vec{p}_1; E, \vec{p}_2) G(E, \vec{p}_2, \vec{x}_2) \right] \alpha^\mu \psi_a(\vec{x}_2), \end{aligned} \quad (35)$$

where $\Gamma(\varepsilon_1, \vec{p}_1; \varepsilon_2, \vec{p}_2)$ is the time component of the renormalized free-electron vertex operator. In order to separate out the IR divergences present in the above expression, we subtract and then re-add the following terms in the brackets above

$$\left[\dots \right] = \left[\dots \mp G^{(a)}(E, \vec{x}_1, \vec{x}_3) G(E, \vec{x}_3, \vec{p}_1) \gamma^0 \left(\Gamma(\varepsilon_a, \vec{p}_1; \varepsilon_a, \vec{p}_2) - \omega \Gamma'(\varepsilon_a, \vec{p}_1; \varepsilon_a, \vec{p}_2) \right) G^{(a)}(E, \vec{p}_2, \vec{x}_2) \right], \quad (36)$$

where $\Gamma'(\varepsilon_a, \vec{p}_1; \varepsilon_a, \vec{p}_2) = d/(d\varepsilon) \Gamma(\varepsilon, \vec{p}_1; \varepsilon, \vec{p}_2)|_{\varepsilon=\varepsilon_a}$. This separates E_{ND2}^P into a regular and two IR-divergent terms,

$$E_{\text{ND2}}^P = E_{\text{ND2}}^P(\mathbf{R}) + E_{\text{ND2}}^P(\text{IR}') + E_{\text{ND2}}^P(\text{IR}). \quad (37)$$

The infrared parts can be factorized and expressed as

$$E_{\text{ND2}}^P(\text{IR}') = (-2) \langle V_g \rangle \langle V_C \gamma^0 \Gamma(\varepsilon_a; \varepsilon_a) \rangle J_3, \quad (38)$$

$$E_{\text{ND2}}^P(\text{IR}) = (-2) \langle V_g \rangle \langle V_C \gamma^0 \Gamma'(\varepsilon_a; \varepsilon_a) \rangle J_2, \quad (39)$$

with integrals J_2 and J_3 defined by Eq. (30) and evaluated in Eqs. (32). The numerical evaluation of the regular (R) part is complicated by the presence of the Coulomb singularity at $q = 0$. This problem is handled by the splitting the vertex operator into the diagonal and the non-diagonal (in momentum) parts, according to Eq. (20). The diagonal part is re-written as

$$\begin{aligned} E_{\text{ND2}}^P(\text{R, diag}) = & 2 \langle V_g \rangle 2i\alpha \int_{C_F} d\omega \int \frac{d\vec{p}}{(2\pi)^3} \int d\vec{x}_1 d\vec{x}_2 d\vec{x}_3 D(\omega, x_{12}) \psi_a^\dagger(\vec{x}_1) \alpha_\mu \\ & \times G(E, \vec{x}_1, \vec{x}_3) G(E, \vec{x}_3, \vec{p}) \gamma^0 \Sigma_R^{(0)'}(E, \vec{p}) G_V(E, \vec{p}, \vec{x}_2) \alpha^\mu \psi_a(\vec{x}_2). \end{aligned} \quad (40)$$

This expression contains only one integration over the momentum and its evaluation is very similar to that for the E_{ND1}^P term. In the nondiagonal part, the integrand is a smooth function of \vec{p}_1 and \vec{p}_2 and the momentum integrations are much easier to calculate numerically. Another important advantage is that the partial-wave expansion of the nondiagonal part converges much faster than that of the diagonal term, so we need to compute less (typically, about 10) partial waves, whereas for the diagonal term we extended the partial-wave expansion up to $|\kappa_{\text{max}}| = 25\text{-}30$.

C. E_{ND3}^P

The third nested derivative contribution is induced by the third line of Fig. 3. Its expression is given by

$$\begin{aligned} E_{\text{ND3}}^P = & \langle V_g \rangle 2i\alpha \int_{C_F} d\omega \int \frac{d\vec{p}}{(2\pi)^3} \int d\vec{x}_1 d\vec{x}_2 D(\omega, x_{12}) \psi_a^\dagger(\vec{x}_1) \alpha_\mu \\ & \times \left[G(E, \vec{x}_1, \vec{p}) \gamma^0 \Sigma_R^{(0)'}(E, \vec{p}) G(E, \vec{p}, \vec{x}_2) - G^{(0)}(E, \vec{x}_1, \vec{p}) \gamma^0 \Sigma_R^{(0)'}(E, \vec{p}) G^{(0)}(E, \vec{p}, \vec{x}_2) \right] \alpha^\mu \psi_a(\vec{x}_2). \end{aligned} \quad (41)$$

In order to separate out the IR divergence, we subtract and then re-add the following contribution in the brackets,

$$\left[\dots \right] = \left[\dots \mp G^{(a)}(E, \vec{x}_1, \vec{p}) \gamma^0 \Sigma_R^{(0)'}(\varepsilon_a, \vec{p}) G^{(a)}(E, \vec{p}, \vec{x}_2) \right]. \quad (42)$$

This transformation separates E_{ND3}^P into the regular and the infrared parts,

$$E_{\text{ND3}}^P = E_{\text{ND3}}^P(\text{R}) + E_{\text{ND3}}^P(\text{IR}). \quad (43)$$

The infrared part is expressed as

$$E_{\text{ND3}}^P(\text{IR}) = \langle V_g \rangle \langle \gamma^0 \Sigma_R^{(0)'}(\varepsilon_a) \rangle J_2. \quad (44)$$

For the numerical evaluation of the regular part, we transform the integrand as

$$\begin{aligned} G(E, \vec{x}_1, \vec{p}) \gamma^0 \Sigma_R^{(0)'}(E, \vec{p}) G(E, \vec{p}, \vec{x}_2) - G^{(0)}(E, \vec{x}_1, \vec{p}) \gamma^0 \Sigma_R^{(0)'}(E, \vec{p}) G^{(0)}(E, \vec{p}, \vec{x}_2) + (\vec{x}_1 \leftrightarrow \vec{x}_2) = \\ = G_V(E, \vec{x}_1, \vec{p}) \frac{1}{\vec{p} - m} \Sigma_R^{(0)'}(E, \vec{p}) \left[G^{(0)}(E, \vec{p}, \vec{x}_2) + G(E, \vec{p}, \vec{x}_2) \right] + (\vec{x}_1 \leftrightarrow \vec{x}_2). \end{aligned} \quad (45)$$

D. E_{OD}^P

The overlapping derivative P -term contribution is represented by the bottom line of Fig. 3. It is given by

$$\begin{aligned} E_{\text{OD}}^P = & 4i\alpha \langle V_g \rangle \int_{C_F} d\omega \int \frac{d\vec{p}_1}{(2\pi)^3} \frac{d\vec{p}_2}{(2\pi)^3} \int d\vec{z} d\vec{y} \frac{e^{-i\vec{q} \cdot \vec{z}}}{\omega^2 - \vec{q}^2 + i0} \psi_a^\dagger(\vec{z}) \alpha_\mu \\ & \times \left[G(E, \vec{z}, \vec{y}) G(E, \vec{y}, \vec{p}_1) - G^{(0)}(E, \vec{z}, \vec{y}) G^{(0)}(E, \vec{y}, \vec{p}_1) \right] \gamma^0 \Gamma_R^\mu(E, \vec{p}_1; \varepsilon_a, \vec{p}_2) \psi_a(\vec{p}_2). \end{aligned} \quad (46)$$

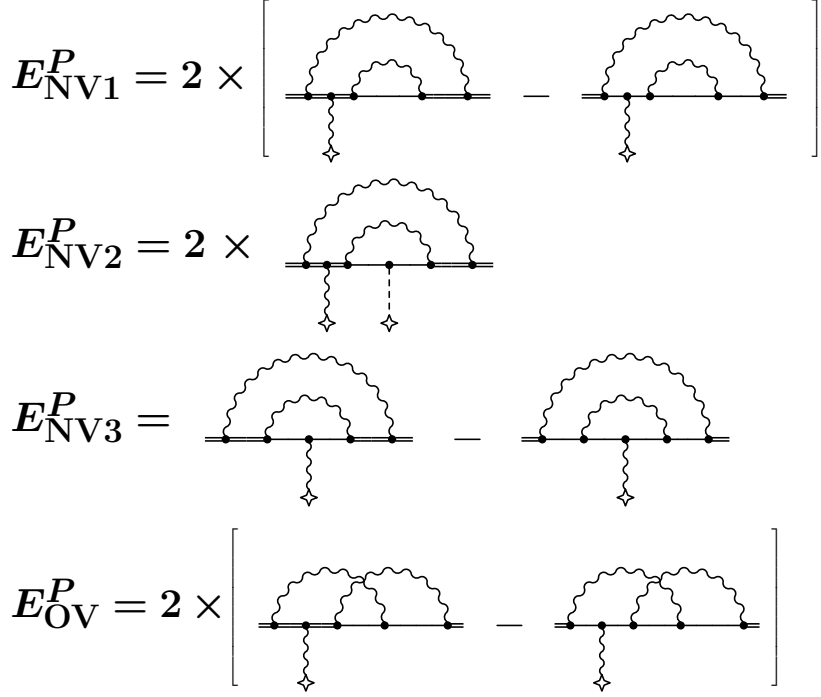


FIG. 4: Diagrammatic representation of the vertex P -term contributions.

In order to remove the IR divergency, we subtract and re-add the following contribution in the brackets:

$$[\dots] = [\dots \mp G^{(a)}(E, \vec{z}, \vec{y}) G^{(a)}(E, \vec{y}, \vec{p}_1)] . \quad (47)$$

This separates E_{OD}^P into the regular (R) and infrared (IR) parts,

$$E_{\text{OD}}^P = E_{\text{OD}}^P(\text{R}) + E_{\text{OD}}^P(\text{IR}) . \quad (48)$$

In the regular contribution, we perform the Wick rotation of the ω integration contour as follows

$$i \sum_{n \neq a} \int_{C_F} d\omega \frac{f_n(\omega)}{(\varepsilon_a - \omega - u\varepsilon_n)^2} = -2 \text{Re} \sum_n \int_0^\infty d\omega \frac{f_n(i\omega)}{(\Delta_{an} - i\omega)^2} , \quad (49)$$

where $\Delta_{an} = \varepsilon_a - \varepsilon_n$. The infrared contribution is given by

$$\begin{aligned} E_{\text{OD}}^P(\text{IR}) &= 4i\alpha \langle V_g \rangle \int_{C_F} d\omega \frac{1}{(-\omega + i0)^2} \int \frac{d\vec{p}_1}{(2\pi)^3} \frac{d\vec{p}_2}{(2\pi)^3} \\ &\times \left(\int d\vec{z} \frac{e^{-i\vec{q} \cdot \vec{z}}}{\omega^2 - \vec{q}^2 + i0} \psi_a^\dagger(\vec{z}) \alpha_\mu \psi_a(\vec{z}) \right) \psi_a^\dagger(\vec{p}_1) \gamma^0 \Gamma_R^\mu(E, \vec{p}_1; \varepsilon_a, \vec{p}_2) \psi_a(\vec{p}_2) . \end{aligned} \quad (50)$$

We observe that the ω integration in the above expression is logarithmically divergent at $\omega \rightarrow 0$. This divergence cancels out when $E_{\text{OD}}^P(\text{IR})$ is considered together with the corresponding contribution from the overlapping vertex part, so we postpone its further evaluation until the vertex term is analysed.

V. VERTEX CONTRIBUTIONS

The vertex P -term contributions are the most complicated ones since they have an additional interaction inserted in the self-energy loop, as compared to the Lamb-shift case. The diagrammatic representation of the vertex P -term contribution is presented in Fig. 4.

A. E_{NV1}^P

The first nested vertex P -term contribution is diagrammatically represented by the uppermost line of Fig. 4. It is given by the expression

$$\begin{aligned} E_{\text{NV1}}^P = & 4i\alpha \int_{C_F} d\omega \int \frac{d\vec{p}}{(2\pi)^3} \int d\vec{x}_1 d\vec{x}_2 d\vec{x}_3 D(\omega, x_{12}) \psi_a^\dagger(\vec{x}_1) \alpha_\mu \\ & \times \left[G(E, \vec{x}_1, \vec{x}_3) V_g(\vec{x}_3) G(E, \vec{x}_3, \vec{p}) \gamma^0 \Sigma_R^{(0)}(E, \vec{p}) G(E, \vec{p}, \vec{x}_2) \right. \\ & \left. - G^{(0)}(E, \vec{x}_1, \vec{x}_3) V_g(\vec{x}_3) G^{(0)}(E, \vec{x}_3, \vec{p}) \gamma^0 \Sigma_R^{(0)}(E, \vec{p}) G^{(0)}(E, \vec{p}, \vec{x}_2) \right] \alpha^\mu \psi_a(\vec{x}_2). \end{aligned} \quad (51)$$

In order to isolate the IR divergencies, we subtract and re-add the following terms in the brackets above,

$$\begin{aligned} [\dots] = & \left[\dots \mp G^{(a)}(E, \vec{x}_1, \vec{x}_3) V_g(\vec{x}_3) G^{(a)}(E, \vec{x}_3, \vec{p}) \gamma^0 \left[\Sigma_R^{(0)}(\varepsilon_a, \vec{p}) - \omega \Sigma_R^{(0)'}(\varepsilon_a, \vec{p}) \right] G^{(a)}(E, \vec{p}, \vec{x}_2) \right. \\ & \left. \mp G^{(a)}(E, \vec{x}_1, \vec{x}_3) V_g(\vec{x}_3) G_{\text{red},a}(\vec{x}_3, \vec{p}) \gamma^0 \Sigma_R^{(0)}(\varepsilon_a, \vec{p}) G^{(a)}(E, \vec{p}, \vec{x}_2) \right], \end{aligned} \quad (52)$$

where $G_{\text{red},a}$ is the reduced Green function for the state a ,

$$G_{\text{red},a}(\vec{x}_1, \vec{x}_2) = \sum_{n \neq a} \frac{\psi_n(\vec{x}_1) \psi_n^\dagger(\vec{x}_2)}{\varepsilon_a - \varepsilon_n}. \quad (53)$$

The above subtraction renders the main contribution IR finite; the subtracted terms are evaluated separately. We thus separate E_{NV1}^P into the sum of the regular (R) and the two infrared (IR', IR) parts,

$$E_{\text{NV1}}^P = E_{\text{NV1}}^P(\text{R}) + E_{\text{NV1}}^P(\text{IR}') + E_{\text{NV1}}^P(\text{IR}). \quad (54)$$

The IR contributions are evaluated as

$$E_{\text{NV1}}^P(\text{IR}') = 2 \langle V_g \rangle \langle \gamma^0 \Sigma_R^{(0)}(\varepsilon_a) \rangle \left[\frac{\alpha}{4\mu} - \frac{\alpha}{4} \sum_{\mu_{a'}} s_{\mu_{a'}} \langle aa' | \alpha_\mu \alpha^\mu x_{12} | a' a \rangle \right], \quad (55)$$

where the expectation value is to be taken with respect to the reference state, $\langle \dots \rangle = \langle a | \dots | a \rangle$, and

$$s_{\mu_{a'}} = \frac{\langle a' | V_g | a' \rangle}{\langle a | V_g | a \rangle} = (-1)^{\mu_a - \mu_{a'}} C_{j_a \mu_{a'}, j_a - \mu_{a'}}^{10} [C_{j_a \mu_a, j_a - \mu_a}^{10}]^{-1}. \quad (56)$$

Furthermore,

$$E_{\text{NV1}}^P(\text{IR}) = 2 \left[\langle V_g \rangle \langle \gamma^0 \Sigma_R^{(0)'}(\varepsilon_a) \rangle + \langle \delta a | \gamma^0 \Sigma_R^{(0)}(\varepsilon_a) | a \rangle \right] \frac{\alpha}{\pi} \left[\ln \frac{\mu}{2} + \gamma + \sum_{\mu_{a'}} s_{\mu_{a'}} \langle aa' | \alpha_\mu \alpha^\mu \ln x_{12} | a' a \rangle \right], \quad (57)$$

where δa is the magnetically perturbed reference-state wave function given by Eq. (5).

B. E_{NV2}^P

The second nested vertex P -term contribution is diagrammatically represented by the second top line in Fig. 4. It is given by

$$\begin{aligned} E_{\text{NV2}}^P = & 4i\alpha \int_{C_F} d\omega \int \frac{d\vec{p}_1}{(2\pi)^3} \frac{d\vec{p}_2}{(2\pi)^3} \int d\vec{x}_1 d\vec{x}_2 d\vec{x}_3 D(\omega, x_{12}) \psi_a^\dagger(\vec{x}_1) V_C(q) \alpha_\mu \\ & \times \left[G(E, \vec{x}_1, \vec{x}_3) V_g(\vec{x}_3) G(E, \vec{x}_3, \vec{p}_1) \gamma^0 \Gamma(E, \vec{p}_1; E, \vec{p}_2) G(E, \vec{p}_2, \vec{x}_2) \right] \alpha^\mu \psi_a(\vec{x}_2). \end{aligned} \quad (58)$$

In order to isolate the IR divergencies, we subtract and then re-add the following terms in the brackets above

$$\begin{aligned} [\dots] = & \left[\dots \mp G^{(a)}(E, \vec{x}_1, \vec{x}_3) V_g(\vec{x}_3) G^{(a)}(E, \vec{x}_3, \vec{p}_1) \gamma^0 \left[\Gamma(\varepsilon_a, \vec{p}_1; \varepsilon_a, \vec{p}_2) - \omega \Gamma'(\varepsilon_a, \vec{p}_1; \varepsilon_a, \vec{p}_2) \right] G^{(a)}(E, \vec{p}_2, \vec{x}_2) \right. \\ & \left. \mp G^{(a)}(E, \vec{x}_1, \vec{x}_3) V_g(\vec{x}_3) G_{\text{red},a}(\vec{x}_3, \vec{p}_1) \gamma^0 \Gamma(\varepsilon_a, \vec{p}_1; \varepsilon_a, \vec{p}_2) G^{(a)}(E, \vec{p}_2, \vec{x}_2) \right], \end{aligned} \quad (59)$$

where $\Gamma'(\varepsilon_a, \vec{p}_1; \varepsilon_a, \vec{p}_2) = d/(d\varepsilon) \Gamma(\varepsilon, \vec{p}_1; \varepsilon, \vec{p}_2)|_{\varepsilon=\varepsilon_a}$. E_{NV2}^P is thus separated into the regular and two infrared parts,

$$E_{\text{NV2}}^P = E_{\text{NV2}}^P(\text{R}) + E_{\text{NV2}}^P(\text{IR}') + E_{\text{NV2}}^P(\text{IR}). \quad (60)$$

The IR contributions are evaluated as follows

$$E_{\text{NV2}}^P(\text{IR}') = 2 \langle V_g \rangle \langle \gamma^0 V_C \Gamma(\varepsilon_a; \varepsilon_a) \rangle \left[\frac{\alpha}{4\mu} - \frac{\alpha}{4} \sum_{\mu_{a'}} s_{\mu_{a'}} \langle aa' | \alpha_\mu \alpha^\mu x_{12} | a' a \rangle \right], \quad (61)$$

and

$$E_{\text{NV2}}^P(\text{IR}) = 2 \left[\langle V_g \rangle \langle \gamma^0 V_C \Gamma'(\varepsilon_a; \varepsilon_a) \rangle + \langle \delta a | \gamma^0 V_C \Gamma(\varepsilon_a; \varepsilon_a) | a \rangle \right] \frac{\alpha}{\pi} \left[\ln \frac{\mu}{2} + \gamma + \sum_{\mu_{a'}} s_{\mu_{a'}} \langle aa' | \alpha_\mu \alpha^\mu \ln x_{12} | a' a \rangle \right]. \quad (62)$$

The regular contribution is finite and can be evaluated numerically as it is. However, it is convenient to separate it into two parts, the one diagonal in the momentum (with $\vec{p}_1 = \vec{p}_2$) and the nondiagonal one, according to Eq. (20). In the diagonal part the integration over one momentum is factorized out. It is transformed to the following form, favourable for numerical evaluation,

$$\begin{aligned} E_{\text{NV2}}^P(\text{diag}) = & -4i\alpha \int_{C_F} d\omega \int \frac{d\vec{p}}{(2\pi)^3} \int d\vec{x}_1 d\vec{x}_2 d\vec{x}_3 D(\omega, x_{12}) \psi_a^\dagger(\vec{x}_1) \alpha_\mu \\ & \times G(E, \vec{x}_1, \vec{x}_3) V_g(\vec{x}_3) G(E, \vec{x}_3, \vec{p}) \gamma^0 \Sigma_R^{(0)'}(E, \vec{p}) G_V(E, \vec{p}, \vec{x}_2) \alpha^\mu \psi_a(\vec{x}_2). \end{aligned} \quad (63)$$

We note that in the above expression the would-be Coulomb singularity of the nuclear potential V_C is absorbed in G_V , where it does not cause any computational difficulties.

C. E_{NV3}^P

The third nested vertex P -term contribution is diagrammatically represented by the third line in Fig. 4. Its expression is

$$\begin{aligned} E_{\text{NV3}}^P = & 2i\alpha \int_{C_F} d\omega \int \frac{d\vec{p}_1}{(2\pi)^3} \frac{d\vec{p}_2}{(2\pi)^3} \int d\vec{x}_1 d\vec{x}_2 D(\omega, x_{12}) \psi_a^\dagger(\vec{x}_1) \alpha_\mu \\ & \times \left[G(E, \vec{x}_1, \vec{p}_1) \gamma^0 \Lambda_{\text{Zee}}(E, \vec{p}_1; E, \vec{p}_2) G(E, \vec{p}_2, \vec{x}_2) - G^{(0)}(E, \vec{x}_1, \vec{p}_1) \gamma^0 \Lambda_{\text{Zee}}(E, \vec{p}_1; E, \vec{p}_2) G^{(0)}(E, \vec{p}_2, \vec{x}_2) \right] \alpha^\mu \psi_a(\vec{x}_2), \end{aligned} \quad (64)$$

where $\Lambda_{\text{Zee}}(\varepsilon_1, \vec{p}_1; \varepsilon_2, \vec{p}_2)$ is the free vertex function with the Zeeman magnetic interaction (which will be referred to as the Zeeman vertex); its explicit expression will be given below in Eq. (70). We separate out the infrared divergences by subtracting and re-adding the following contribution in the brackets,

$$[\dots] = \left[\dots \mp G^{(a)}(E, \vec{x}_1, \vec{p}_1) \gamma^0 \Lambda_{\text{Zee}}(\varepsilon_a, \vec{p}_1; \varepsilon_a, \vec{p}_2) G^{(a)}(E, \vec{p}_2, \vec{x}_2) \right], \quad (65)$$

which separates Eq. (64) into two parts,

$$E_{\text{NV3}}^P = E_{\text{NV3}}^P(\text{R}) + E_{\text{NV3}}^P(\text{IR}). \quad (66)$$

The IR contribution is evaluated as

$$E_{\text{NV3}}^P(\text{IR}) = \langle \gamma^0 \Lambda_{\text{Zee}}(\varepsilon_a; \varepsilon_a) \rangle \frac{\alpha}{\pi} \left[\ln \frac{\mu}{2} + \gamma + \sum_{\mu_{a'}} s_{\mu_{a'}} \langle aa' | \alpha_\mu \alpha^\mu \ln x_{12} | a' a \rangle \right]. \quad (67)$$

We now turn to the Zeeman vertex function Λ_{Zee} . The straightforward representation of its matrix element with the Dirac wave functions is given by Eq. (15) of Ref. [36]. This representation involves the gradient of the Dirac δ function and is cumbersome to work with. In the present work we choose to follow Ref. [37] and to use the regularized version of the Zeeman magnetic interaction. Specifically, we introduce a small regulator parameter ρ and define the regularized magnetic potential $V_{g,\rho}$ in the coordinate space as

$$V_{g,\rho}(\vec{r}) = \frac{1}{\mu_a} [\vec{r} \times \vec{\alpha}]_z e^{-(\rho r/2)^2}, \quad (68)$$

which obviously approaches V_g as $\rho \rightarrow 0$. Performing the Fourier transform, we obtain the matrix element of $V_{g,\rho}$ with the Dirac wave functions in momentum space as

$$\langle n | V_{g,\rho} | m \rangle = \int d\vec{x} \psi_n^\dagger(\vec{x}) V_{g,\rho}(\vec{x}) \psi_m(\vec{x}) = (-4\pi i) A_\rho \int \frac{d\vec{p}_1}{(2\pi)^3} \frac{d\vec{p}_2}{(2\pi)^3} \psi_n^\dagger(\vec{p}_1) \gamma^0 [\vec{q} \times \vec{\gamma}]_z e^{-q^2/\rho^2} \psi_m(\vec{p}_2), \quad (69)$$

where $\vec{q} = \vec{p}_1 - \vec{p}_2$, $q = |\vec{q}|$, and $A_\rho = 4\pi^{1/2}/(\mu_a \rho^5)$. Analogously, the matrix element of the Zeeman vertex between the Dirac states in momentum space is given by

$$\langle n | \gamma^0 \Lambda_{\text{Zee}}(\varepsilon_1, \varepsilon_2) | m \rangle = (-4\pi i) A_\rho \int \frac{d\vec{p}_1}{(2\pi)^3} \frac{d\vec{p}_2}{(2\pi)^3} \psi_n^\dagger(\vec{p}_1) \gamma^0 [\vec{q} \times \vec{\Gamma}(\varepsilon_1, \vec{p}_1; \varepsilon_2, \vec{p}_2)]_z e^{-q^2/\rho^2} \psi_m(\vec{p}_2), \quad (70)$$

where $\vec{\Gamma}(\varepsilon_1, \vec{p}_1; \varepsilon_2, \vec{p}_2)$ is the vector part of the renormalized one-loop vertex function defined in Appendix A of Ref. [38]. Note that the regularized Zeeman vertex has essentially the same form as the vertex with the magnetic dipole hyperfine interaction, see Eq. (28) of Ref. [32]. The angular integrations of expressions with the Zeeman vertex in momentum space are detailed out in Appendix A.

In actual numerical calculations, we found that when reasonably small values of the regulator ($\rho \approx 10^{-4}$) are used, the dependence of results on the regulator value is negligible. In addition, the integration over one of the two momenta (say, \vec{p}_2) is greatly simplified by the fact that the integrand is strongly peaked around the point $\vec{p}_2 = \vec{p}_1$, so that the integration is actually needed only over a small region $\vec{p}_2 \approx \vec{p}_1$.

D. E_{OV}^P

The overlapping vertex P -term contribution is represented by the bottom line of Fig. 4 and is given by

$$E_{\text{OV}}^P = -4i\alpha \int_{C_F} d\omega \int \frac{d\vec{p}_1}{(2\pi)^3} \frac{d\vec{p}_2}{(2\pi)^3} \int d\vec{z} d\vec{y} \frac{e^{-i\vec{q} \cdot \vec{z}}}{\omega^2 - \vec{q}^2 + i0} \psi_a^\dagger(\vec{z}) \alpha_\mu \times \left[G(E, \vec{z}, \vec{y}) V_g(\vec{y}) G(E, \vec{y}, \vec{p}_1) - G^{(0)}(E, \vec{z}, \vec{y}) V_g(\vec{y}) G^{(0)}(E, \vec{y}, \vec{p}_1) \right] \gamma^0 \Gamma_R^\mu(E, \vec{p}_1; \varepsilon_a, \vec{p}_2) \psi_a(\vec{p}_2). \quad (71)$$

In order to separate out the IR divergency, we subtract and re-add the following contribution in the brackets

$$[\dots] = [\dots \mp G^{(a)}(E, \vec{z}, \vec{y}) V_g(\vec{y}) G^{(a)}(E, \vec{y}, \vec{p}_1)], \quad (72)$$

thus separating E_{OV}^P into the regular (R) and infrared (IR) parts,

$$E_{\text{OV}}^P = E_{\text{OV}}^P(\text{R}) + E_{\text{OV}}^P(\text{IR}). \quad (73)$$

In the regular contribution, we perform the Wick rotation of the ω integration contour, separating pole contributions as follows (assuming that a is the ground state)

$$i \sum_{n_1 n_2 \neq aa} \int_{C_F} d\omega \frac{f_{n_1 n_2}(\omega)}{(\varepsilon_a - \omega - u\varepsilon_{n_1})(\varepsilon_a - \omega - u\varepsilon_{n_2})} = -2 \left\{ -\frac{\pi}{2} \sum_{n_2 \neq a} \frac{f_{a n_2}(0)}{\Delta_{a n_2}} - \frac{\pi}{2} \sum_{n_1 \neq a} \frac{f_{n_1 a}(0)}{\Delta_{a n_1}} + \text{Re} \sum_{n_1 n_2 \neq aa} \int_0^\infty d\omega \frac{f_{n_1 n_2}(i\omega)}{(\Delta_{a n_1} - i\omega)(\Delta_{a n_2} - i\omega)} \right\}, \quad (74)$$

where $\Delta_{a n} = \varepsilon_a - \varepsilon_n$ and in the summation over n_1 and n_2 the term with $(n_1, n_2) = (a, a)$ is omitted. The angular integration in E_{OV}^P is quite complicated and is detailed out in Appendix B. The IR contribution is transformed as

$$E_{\text{OV}}^P(\text{IR}) = -4i\alpha \int_{C_F} d\omega \frac{1}{(-\omega + i0)^2} \int \frac{d\vec{p}_1}{(2\pi)^3} \frac{d\vec{p}_2}{(2\pi)^3} \sum_{\mu_a'} \langle a' | V_g | a' \rangle$$

$$\times \left(\int d\vec{z} \frac{e^{-i\vec{q}\cdot\vec{z}}}{\omega^2 - \vec{q}^2 + i0} \psi_a^\dagger(\vec{z}) \alpha_\mu \psi_{a'}(\vec{z}) \right) \psi_{a'}^\dagger(\vec{p}_1) \gamma^0 \Gamma_R^\mu(E, \vec{p}_1; \varepsilon_a, \vec{p}_2) \psi_a(\vec{p}_2), \quad (75)$$

where the state a' differs from the reference state a only by the angular-momentum projection $\mu_{a'}$.

The IR divergence present in the above expression cancels out when $E_{\text{OV}}^P(\text{IR})$ is considered together with the corresponding contribution from the overlapping derivative term, $E_{\text{OD}}^P(\text{IR})$. We, therefore, introduce the total overlapping IR contribution as

$$E_{\text{OVD}}^P(\text{IR}) = E_{\text{OV}}^P(\text{IR}) + E_{\text{OD}}^P(\text{IR}). \quad (76)$$

In order to calculate $E_{\text{OVD}}^P(\text{IR})$ numerically, we need to deform the ω integration contour to be parallel to the imaginary axis. However, the standard Wick rotation is not possible in this case. The situation is somewhat similar to that for the vertex + reducible contribution for the one-loop self-energy correction to the g factor. In Ref. [37], it was suggested to use a small numerical regularization parameter to shift the reference-state energy, thus removing the infrared divergence of the integral. The idea was to perform the Wick rotation of the regularized expression and then evaluate the limit numerically by decreasing the regularization parameter. In the present work, we use a similar but somewhat different approach. We introduce a small regularization parameter ϵ that shifts the Wick-rotated ω integration contour, $(-i\infty, i\infty) \rightarrow (\epsilon - i\infty, \epsilon + i\infty)$. We obtain the regularized expression

$$E_{\text{OVD}}^P(\text{IR}, \epsilon) = 8\alpha \text{Re} \int_0^\infty dw \frac{1}{\omega^2} \int \frac{d\vec{p}_1}{(2\pi)^3} \frac{d\vec{p}_2}{(2\pi)^3} \left[\sum_{\mu_{a'}} \langle a' | V_g | a' \rangle - \delta_{\mu_a \mu_{a'}} \langle a | V_g | a \rangle \right] \times \left(\int d\vec{z} \frac{e^{-i\vec{q}\cdot\vec{z}}}{\omega^2 - \vec{q}^2} \psi_a^\dagger(\vec{z}) \alpha_\mu \psi_{a'}(\vec{z}) \right) \psi_{a'}^\dagger(\vec{p}_1) \gamma^0 \Gamma_R^\mu(\varepsilon_a - \omega, \vec{p}_1; \varepsilon_a, \vec{p}_2) \psi_a(\vec{p}_2) \Big|_{\omega=\epsilon+iw}. \quad (77)$$

Here, the integrand is supposed to be evaluated for $\omega = \epsilon + iw$. The final infrared contribution is determined by numerically evaluating the limit $\epsilon \rightarrow 0$,

$$E_{\text{OVD}}^P(\text{IR}) = \lim_{\epsilon \rightarrow 0+} E_{\text{OVD}}^P(\text{IR}, \epsilon). \quad (78)$$

Specifically, we perform calculations for several values of the regulator parameter (typically, about 10 values in the range between 10^{-3} and 10^{-2}) and obtain the final IR contribution by a polynomial fit of the limit $\epsilon \rightarrow 0$.

It is important that the limit in Eq. (78) is approached from the positive values of the regulator. It is possible to use the negative values of the regulator as well, but then one needs to add the pole contribution at $\omega = 0$, according to the identity

$$-2 \lim_{\epsilon \rightarrow 0+} \text{Re} \int_0^\infty dw \frac{f(\epsilon + iw)}{(\epsilon + iw)^2} = -2 \lim_{\epsilon \rightarrow 0-} \text{Re} \int_0^\infty dw \frac{f(\epsilon + iw)}{(\epsilon + iw)^2} - 2\pi f'(0). \quad (79)$$

We checked the fulfillment of this identity numerically, which served as an additional check of our numerical procedures. It is interesting that for the one-loop self-energy correction to the g factor, the pole contribution vanishes, so that the limit $\epsilon \rightarrow 0$ can be approached from both the positive and the negative sides, with the same result.

We also mention that the above contour with $\epsilon > 0$ can be considered as a variant of our standard contour C_{LH} , in which the length of the low-energy part of the contour (and, therefore, the corresponding low-energy contribution) approaches zero.

VI. ADDITIONAL CONTRIBUTION

The additional P -term contribution is introduced in this work in order to make the whole P term IR finite. We will demonstrate that the IR divergences in individual P -term contributions discussed in the previous sections disappear when combined with (parts of) contributions referred to as the loop-after-loop reducible part in Ref. [26] and given by Eqs. (6.17)-(6.20) of that work. Specifically, we define the additional P -term contribution as

$$E_{\text{ADD}}^P = \left\{ \langle V_g \rangle \langle \gamma^0 \Sigma_R^{(0)'}(\varepsilon_a) \rangle + \langle \gamma^0 \Lambda_{\text{Zee}}(\varepsilon_a; \varepsilon_a) \rangle + 2 \langle \delta a | \gamma^0 [\Sigma_R^{(0)}(\varepsilon_a) + V_C \Gamma(\varepsilon_a; \varepsilon_a)] | a \rangle \right\} \langle \gamma^0 [\Sigma'(\varepsilon_a) - \Sigma_R^{(0)'}(\varepsilon_a)] \rangle. \quad (80)$$

We split E_{ADD}^P into the regular and IR parts, $E_{\text{ADD}}^P = E_{\text{ADD}}^P(\text{R}) + E_{\text{ADD}}^P(\text{IR})$, by subtracting and re-adding in the matrix element of the self-energy operator $\Sigma(\varepsilon)$ the contribution of the reference states $\Sigma^{(a)}(\varepsilon)$,

$$\langle \gamma^0 \left[\Sigma'(\varepsilon_a) - \Sigma_R^{(0)'}(\varepsilon_a) \right] \rangle = \langle \gamma^0 \left[\Sigma'(\varepsilon_a) - \Sigma_R^{(0)'}(\varepsilon_a) - \Sigma^{(a)'}(\varepsilon_a) \right] \rangle + \langle \gamma^0 \Sigma^{(a)'}(\varepsilon_a) \rangle. \quad (81)$$

Here,

$$\langle \gamma^0 \Sigma^{(a)}(\varepsilon) \rangle = \frac{i}{2\pi} \int_{-\infty}^{\infty} d\omega \sum_{\mu_{a'}} \frac{\langle aa' | I(\omega) | a' a \rangle}{\varepsilon - \omega - \varepsilon_a + i0}. \quad (82)$$

Using Eq. (30), we immediately evaluate the infrared contribution as

$$E_{\text{ADD}}^P(\text{IR}) = - \left\{ \langle V_g \rangle \langle \gamma^0 \Sigma_R^{(0)'}(\varepsilon_a) \rangle + \langle \gamma^0 \Lambda_{\text{Zee}}(\varepsilon_a; \varepsilon_a) \rangle + 2 \langle \delta a | \gamma^0 [\Sigma_R^{(0)}(\varepsilon_a) + V_C \Gamma(\varepsilon_a; \varepsilon_a)] | a \rangle \right\} J_2. \quad (83)$$

The regular part $E_{\text{ADD}}^P(\text{R})$ is calculated to a very high accuracy by a straightforward generalization of the method developed for the one-loop self-energy in Ref. [39].

VII. TOTAL P TERM

Finally, the total P -term is given by the sum of all contributions,

$$\begin{aligned} E_P = & E_{\text{NW1}}^P + E_{\text{NW2}}^P + E_{\text{OW}}^P + E_{\text{ND1}}^P + E_{\text{ND2}}^P + E_{\text{ND3}}^P \\ & + E_{\text{NV1}}^P + E_{\text{NV2}}^P + E_{\text{NV3}}^P + E_{\text{OD}}^P + E_{\text{OV}}^P + E_{\text{ADD}}^P. \end{aligned} \quad (84)$$

The P term E_P is finite. The IR divergence in individual contributions disappears when all terms are added together. The cancelation of divergences between the individual contributions is demonstrated in Table I.

VIII. NUMERICAL CALCULATIONS

The P term consists of many different contributions whose computation is complicated and time-consuming.

In order to obtain reliable numerical results, we had to perform numerous cross-checks of our numerical procedures and test calculations, of which some have already been mentioned. Others will be discussed in this section.

We performed a set of test calculations, in which we reduced our two-loop P -term contributions to less complicated one-loop diagrams. More specifically, we observed that in each of the P -term contributions, if we “collapse” the inner one-loop subgraph and replace it by the corresponding vertex, the result can be converted back to the coordinate space and computed by standard methods developed for calculations of one-loop self-energy corrections. Specifically, the replacements are $\Sigma_R^{(0)}(\varepsilon, \vec{p}) \rightarrow \gamma^0$, $\Gamma_R^\mu(\varepsilon_1, \vec{p}_1; \varepsilon_2, \vec{p}_2) \rightarrow \gamma^\mu$, $\Lambda_{\text{Zee}}(\varepsilon_1, \vec{p}_1; \varepsilon_2, \vec{p}_2) \rightarrow \gamma^0 V_g$. These simplifications give a very valuable opportunity to check our numerical procedures for the two-loop P -term contributions by reducing them to one-loop calculations which can be independently checked. We did these tests for all P -term contributions discussed in the previous sections.

As an illustration, let us now examine a test calculation carried out for the most complicated P -term contribution, specifically, the vertex overlapping term E_{OV}^P . After performing the above mentioned replacement $\Gamma_R^\mu(\varepsilon_1, \vec{p}_1; \varepsilon_2, \vec{p}_2) \rightarrow \gamma^\mu$, the regular part of E_{OV}^P becomes $E_{\text{OV}}^P(\text{R}) \rightarrow \delta E_1$, where

$$\begin{aligned} \delta E_1 = & -4i\alpha \int_{C_F} d\omega \int \frac{d\vec{p}_1}{(2\pi)^3} \frac{d\vec{p}_2}{(2\pi)^3} \int d\vec{z} d\vec{y} \frac{e^{-i\vec{q} \cdot \vec{z}}}{\omega^2 - \vec{q}^2 + i0} \psi_a^\dagger(\vec{z}) \alpha_\mu \\ & \times \left[G(E, \vec{z}, \vec{y}) V_g(\vec{y}) G(E, \vec{y}, \vec{p}_1) - G^{(0)}(E, \vec{z}, \vec{y}) V_g(\vec{y}) G^{(0)}(E, \vec{y}, \vec{p}_1) - G^{(a)}(E, \vec{z}, \vec{y}) V_g(\vec{y}) G^{(a)}(E, \vec{y}, \vec{p}_1) \right] \alpha^\mu \psi_a(\vec{p}_2). \end{aligned} \quad (85)$$

On one hand, δE_1 can be calculated according to Eq. (85) by the numerical procedure developed for $E_{\text{OV}}^P(\text{R})$. On the other hand, the above expression can be transformed to the fully coordinate representation, with the result

$$\begin{aligned} \delta E_1 = & -4i\alpha \int_{C_F} d\omega \int d\vec{z} d\vec{y} d\vec{x} D(\omega, |\vec{z} - \vec{x}|) \psi_a^\dagger(\vec{z}) \alpha_\mu \\ & \times \left[G(E, \vec{z}, \vec{y}) V_g(\vec{y}) G(E, \vec{y}, \vec{x}) - G^{(0)}(E, \vec{z}, \vec{y}) V_g(\vec{y}) G^{(0)}(E, \vec{y}, \vec{x}) - G^{(a)}(E, \vec{z}, \vec{y}) V_g(\vec{y}) G^{(a)}(E, \vec{y}, \vec{x}) \right] \alpha^\mu \psi_a(\vec{x}). \end{aligned} \quad (86)$$

Eq. (86) can be identified as the (1+)-potential vertex

contribution to the self-energy correction to the g fac-

TABLE I: Cancelation of infrared-divergent parts of individual P -term contributions.

Contribution	$\times \frac{\alpha}{4\mu}$	$\times \frac{\alpha}{\pi} (\ln \frac{\mu}{2} + \gamma)$
E_{ND1}^P	$(-2) \langle V_g \rangle \langle \gamma^0 \Sigma_R^{(0)}(\varepsilon_a) \rangle$	$(-2) \langle V_g \rangle \langle \gamma^0 \Sigma_R^{(0)'}(\varepsilon_a) \rangle$
E_{ND2}^P	$(-2) \langle V_g \rangle \langle \gamma^0 V_C \Gamma(\varepsilon_a; \varepsilon_a) \rangle$	$(-2) \langle V_g \rangle \langle \gamma^0 V_C \Gamma'(\varepsilon_a; \varepsilon_a) \rangle$
E_{ND3}^P		$\langle V_g \rangle \langle \gamma^0 \Sigma_R^{(0)'}(\varepsilon_a) \rangle$
E_{NV1}^P	$2 \langle V_g \rangle \langle \gamma^0 \Sigma_R^{(0)}(\varepsilon_a) \rangle$	$2 \langle V_g \rangle \langle \gamma^0 \Sigma_R^{(0)'}(\varepsilon_a) \rangle + 2 \langle \delta a \gamma^0 \Sigma_R^{(0)}(\varepsilon_a) a \rangle$
E_{NV2}^P	$2 \langle V_g \rangle \langle \gamma^0 V_C \Gamma(\varepsilon_a; \varepsilon_a) \rangle$	$2 \langle V_g \rangle \langle \gamma^0 V_C \Gamma'(\varepsilon_a; \varepsilon_a) \rangle + 2 \langle \delta a \gamma^0 V_C \Gamma(\varepsilon_a; \varepsilon_a) a \rangle$
E_{NV3}^P		$\langle \gamma^0 \Lambda_{\text{Zee}}(\varepsilon_a; \varepsilon_a) \rangle$
E_{ADD}^P		$-\langle V_g \rangle \langle \gamma^0 \Sigma_R^{(0)'}(\varepsilon_a) \rangle - \langle \gamma^0 \Lambda_{\text{Zee}}(\varepsilon_a; \varepsilon_a) \rangle - 2 \langle \delta a \gamma^0 [\Sigma_R^{(0)}(\varepsilon_a) + V_C \Gamma(\varepsilon_a; \varepsilon_a)] a \rangle$
Sum	0	0

TABLE II: Results of the test calculation: $\delta E_1 \times \alpha / (4\pi)$ computed in the mixed momentum-coordinate representation, Eq. (85), and in the fully coordinate representation, Eq. (86). Units are 10^{-6} .

$ \kappa $	Mixed	Coordinate
1	1.63831	1.63827
2	-0.03713	-0.03713
3	-0.04940	-0.04940
4	-0.02442	-0.02442
5	-0.01327	-0.01327
6...15	-0.02509	-0.02511
16... ∞	-0.00377 (23)	-0.00382 (2)
Sum	1.48518 (23)	1.48513 (2)

tor, which was encountered in our previous calculations [11, 36]. Computation of this expression in coordinate space is relatively straightforward and was performed by numerical routines developed in Ref. [36]. Numerical results of our test calculations of δE_1 carried out in the mixed representation and in the coordinate representation are presented in Table II. We observe that our computations in the mixed representation reproduce well the (much more accurate) values obtained in the coordinate representation. This comparison proves that we are able to keep the momentum integrations in the mixed momentum-coordinate representation well under control. It should be pointed out that the two computations used different integration contours for the ω integration. In the mixed representation, we used the integration over the imaginary axis, whereas in the coordinate representation, we used our standard C_{LH} integration contour [35]. So, this test also checks the correctness of our treatment of the pole contributions in the mixed representation.

Another important test of our numerical procedures was the check of cancelation of the $J = 0$ multipole part of infrared-divergent contributions. More specifically, the IR' and IR contributions contain an expansion over the

multipoles $J \geq 0$ of the photon propagator. It was shown [26] that only the lowest multipole $J = 0$ part is diverging, whereas the higher-order multipoles $J > 0$ are actually finite. (For the $1s$ reference state considered here, there is only one other multipole contribution, $J = 1$.) It was also shown [26] that the $J = 0$ multipole contributions cancel *exactly* in the total sum, both the divergent parts and finite remainders. In the present work we checked these statements numerically.

Our numerical results obtained for individual P -term contributions for the $1s$ state of hydrogen-like tin ($Z = 50$) and bismuth ($Z = 83$) are presented in Table III for $Z = 50$ and Table IV for $Z = 83$. The tables present numerical results for the IR' and IR contributions in two variants (the left and right subcolumns). The left subcolumns (labeled “ $J \geq 0$ ”) show results with the $J = 0$ multipole included, whereas the right subcolumns (labeled “ $J > 0$ ”) presents results with the $J = 0$ multipole excluded. We observe that sums of both subcolumns are the same, both for the IR and the IR' contribution (although the $J \geq 0$ case leads to much larger numerical cancelations). This proves that the $J = 0$ multipole terms cancel each other identically, as they should.

Furthermore, we used the fact that the $J = 1$ multipole contributions of the IR' and IR terms are finite for an additional test. We performed calculations of the IR' and IR terms for the nested diagrams in two different ways. First, we computed the $J = 1$ contributions by the formulas presented above, with the ω integration calculated analytically. Second, we computed the same contributions by the general routine developed for the regular parts, with the ω integration performed numerically. Perfect agreement was observed in all cases. As a matter of fact, the explicit separation of the IR contributions was not even necessary. We could have removed all IR subtractions and just dropped the $J = 0$ multipole in our general codes computing the regular contributions, and the total result would be the same. However, we found it safer to compute the IR contributions separately and check their cancelation explicitly.

For the overlapping-diagram IR contributions, we were not able to carry out the analytical calculations of the ω integrals and had to rely on the numerical integration method. In order to cross-check this part, we used numerical integration with both positive and negative values of the regulator ϵ , as discussed in the previous section.

The numerical approach used in this work for computing Feynman diagrams in the mixed momentum-coordinate representation closely follows the procedure described in Ref. [31] and is therefore not discussed further here.

IX. RESULTS

Tables III and IV summarize our numerical results obtained for individual P -term contributions for the $1s$ state of hydrogen-like tin ($Z = 50$) and bismuth ($Z = 83$). Our calculations were performed for the point nuclear model. Each P -term contribution is separated into the infrared IR', IR and the regular R parts. The infrared contributions are calculated in two variants, with all multipoles of the photon propagator included (" $J \geq 0$ " columns) and with the $J = 0$ multipole excluded (" $J > 0$ " columns), see the discussion in the previous section. The sum of all individual IR' and IR contributions in the $J \geq 0$ and $J > 0$ columns is the same within the numerical uncertainty, which served as an important cross-check of our calculations.

We note large numerical cancelation between individual P -term contributions, particularly pronounced for smaller values of Z . For instance, for $Z = 50$, the sum of absolute values of all P -term contributions is by about three orders of magnitude larger than the final result. This cancelation highlights the necessity of carefully controlling numerical uncertainties at intermediate stages of the computation. Any small mistake in a single contribution would have a greatly magnified impact on the final result.

The dominant numerical uncertainty in our computations comes from the overlapping vertex contribution E_{OV}^P . The limitation was due to the fact that we were able to extend the partial-wave summation only up to $|\kappa_{\text{max}}| = 15$. For larger values of κ , the computation of the angular-momentum coefficients described in Appendix B becomes unstable due to severe numerical cancelations arising for $q \rightarrow 0$. Even with extended-precision arithmetic for the angular-momentum coefficients, we were unable to extend the partial-wave summation beyond this point.

Final numerical results of our calculation of the P -term contribution to the two-loop self-energy correction to the $1s$ g -factor of H-like ions with $Z \geq 50$ are presented in Table V.

In Table VI we summarize all contributions to the SESE correction for the bound-electron g factor of H-like tin ion ($Z = 50$), which was recently measured [7]. Our final result of $-4.10(2) \times 10^{-6}$ is in good agreement

with previous estimations of this correction based on the $Z\alpha$ expansion [7, 13–16], $-4.3(3) \times 10^{-6}$, and improves its accuracy by an order of magnitude.

Our first complete results for the SESE correction in H-like tin were reported in our recent Letter [28]. They improved the theoretical accuracy for the g factor of H-like tin by an order of magnitude over the previous theoretical value reported in Ref. [7]. The updated theoretical result showed a mild tension of 2.1σ with the experimental value. A potential cause for the tension could be an underestimated uncertainty of the currently accepted nuclear charge radius of ^{118}Sn , as listed in the tabulation [40]. This interpretation is supported by the recent criticism by Ohayon [41], who argued that the model dependence of the nuclear charge distribution had not been properly accounted for in Ref. [40] and their uncertainties should be substantially increased.

X. SUMMARY AND OUTLOOK

We presented a detailed description of our calculational approach developed for the so-called P -term part of the two-loop self-energy correction for the bound-electron g factor. The P -term consists of Feynman diagrams that need be treated in a mixed momentum-coordinate representation. A detailed analysis of infrared divergencies present in individual P -term contributions was carried out, and their cancelation was explicitly demonstrated. Explicitly finite formulas were derived, suitable for numerical computations. Numerical calculations of the P term were carried out for the g factor of the $1s$ state of H-like ions with the nuclear charges $Z \geq 50$. The results obtained for the $Z = 50$ allowed us to improve the theoretical accuracy for the g factor of H-like tin and enabled a stringent test of the magnetic sector of bound-state QED theory.

In future studies, it will be necessary to extend our calculations of the SESE correction to ions other than tin. On the one hand, upcoming measurements on g -factors of heavy H-like ions are planned by the ALPHA-TRAP experiment [42], which require nonperturbative (in $Z\alpha$) calculations of the SESE correction. On the other hand, high-precision experimental results are already available for g factors of lower- Z ions [4–6], where the SESE correction constitutes a dominant source of theoretical uncertainty. An extension of the present calculations to the smaller nuclear charges $Z < 50$ is likely to be rather challenging because of the slower convergence of the partial-wave expansion and the stronger numerical cancelations. Possible strategies to overcome these difficulties could include the partial-wave convergence acceleration scheme [43], recently generalized to the two-loop Lamb-shift calculations [24, 25], as well as the use of the Coulomb gauge, which has proven to be highly effective in one-loop self-energy calculations [44].

TABLE III: Numerical results for the finite parts of individual P -term contributions, for $Z = 50$, in units of 10^{-6} .

Term	IR'		IR		R	Sum
	$J \geq 0$	$J > 0$	$J \geq 0$	$J > 0$		
NW1	—	—	—	—	1.8363 (2)	1.8363 (2)
NW2	—	—	—	—	-1.2483 (1)	-1.2483 (1)
OW	—	—	—	—	0.5624	0.5624
ND1	-21.1790	-0.7672	-36.3756	-0.9667	-25.0694 (6)	-26.8033 (6)
ND2	14.0526	0.5090	-19.7867	-0.5258	-12.0327 (4)	-12.0495 (4)
ND3	—	—	18.1878	0.4833	14.5088	14.9921
NV1	20.1561	-0.2557	38.0456	-0.3494	22.5079 (6)	21.9028 (6)
NV2	-13.3739	0.1697	18.9901	-0.1744	12.5088 (4)	12.5041 (4)
NV3	—	—	-11.7391	0.1078	-11.6888 (4)	-11.5810 (4)
OD + OV	—	—	0.3602	0.3602	1.7801 (40)	2.1403 (40)
ADD	—	—	-8.9860	-0.2388	-2.2846	-2.5234
Sum	-0.3442	-0.3442	-1.3037	-1.3038	1.3805 (42)	-0.2674 (42)

TABLE IV: Numerical results for the finite parts of individual P -term contributions, for $Z = 83$, in units of 10^{-6} .

Term	IR'		IR		R	Sum
	$J \geq 0$	$J > 0$	$J \geq 0$	$J > 0$		
NW1	—	—	—	—	3.1250 (5)	3.1250 (5)
NW2	—	—	—	—	-3.8740 (9)	-3.8740 (9)
OW	—	—	—	—	-0.0502 (1)	-0.0502 (1)
ND1	-19.5278	-1.7893	-10.7545	-1.1351	-11.1065 (2)	-14.0309 (2)
ND2	15.9184	1.4586	-8.9433	-0.9439	-5.4600 (10)	-4.9453 (10)
ND3	—	—	5.3772	0.5676	5.9359 (1)	6.5035 (1)
NV1	17.1421	-0.5964	11.6501	-0.4770	9.1974 (6)	8.1240 (6)
NV2	-13.9737	0.4862	9.1883	-0.3762	7.0464 (11)	7.1564 (11)
NV3	—	—	-2.0729	0.0849	-4.4407 (1)	-4.3558 (1)
OD + OV	—	—	0.2691	0.2691	1.3896 (21)	1.6587 (21)
ADD	—	—	-7.5185	-0.7936	-1.3635	-2.1571
Sum	-0.4410	-0.4410	-2.8044	-2.8042	0.3995 (28)	-2.8459 (28)

TABLE V: The P term for the $1s$ g factor of H-like ions, in units of 10^{-6} .

Z	E_P
50	-0.2674 (42)
60	-0.9498 (83)
70	-1.7257 (31)
83	-2.8459 (28)
92	-3.7369 (115)

ACKNOWLEDGMENT

This work is funded by the Deutsche Forschungsgemeinschaft (DFG, German Research Foundation) under the Collaborative Research Centre, Project-ID No. 273811115, SFB 1225 ISOQUANT.

[1] H. Häffner, T. Beier, N. Hermanspahn, H.-J. Kluge, W. Quint, S. Stahl, J. Verdú, and G. Werth, Phys. Rev. Lett. **85**, 5308 (2000), URL <https://doi.org/10.1103/PhysRevLett.85.5308>.

[2] J. Verdú, S. Djekić, S. Stahl, T. Valenzuela, M. Vogel, G. Werth, T. Beier, H.-J. Kluge, and W. Quint, Phys. Rev. Lett. **92**, 093002 (2004), URL <https://doi.org/10.1103/PhysRevLett.92.093002>.

[3] S. Sturm, A. Wagner, B. Schabinger, J. Zatorski, Z. Harman, W. Quint, G. Werth, C. H. Keitel, and K. Blaum, Phys. Rev. Lett. **107**, 023002 (2011), URL <https://doi.org/10.1103/PhysRevLett.107.023002>.

[4] S. Sturm, A. Wagner, M. Kretzschmar, W. Quint, G. Werth, and K. Blaum, Phys. Rev. A **87**,

TABLE VI: Two-loop self-energy contributions to the 1s bound-electron g -factor of H-like tin, in units of 10^{-6} .

Term	Value	Ref.
F-term	-4.0835 (1)	[27]
LAL	0.1086 (35)	[27, 28]
M-term	0.143 (17)	[28]
P-term	-0.2674 (42)	This work
Sum	-4.099 (19)	This work, [28]
$Z\alpha$ -expansion	-4.25 (30)	[7, 13, 15]

030501(R) (2013), URL <http://link.aps.org/doi/10.1103/PhysRevA.87.030501>.

[5] S. Sturm, F. Köhler, J. Zatorski, A. Wagner, Z. Harman, G. Werth, W. Quint, C. H. Keitel, and K. Blaum, *Nature* **506**, 467–470 (2014), URL <https://doi.org/10.1038/nature13026>.

[6] T. Sailer, V. Debierre, Z. Harman, F. Heiße, C. König, J. Morgner, B. Tu, A. V. Volotka, C. H. Keitel, K. Blaum, et al., *Nature* **606**, 479 (2022), URL <https://doi.org/10.1038/s41586-022-04807-w>.

[7] J. Morgner, B. Tu, C. König, T. Sailer, F. Heiße, H. Bekker, B. Sikora, C. Lyu, V. Yerokhin, Z. Harman, et al., *Nature* **622**, 53 (2023), URL <https://doi.org/10.1038/s41586-023-06453-2>.

[8] H. Persson, S. Salomonson, P. Sunnergren, and I. Lindgren, *Phys. Rev. A* **56**, R2499 (1997), URL <https://doi.org/10.1103/PhysRevA.56.R2499>.

[9] T. Beier, *Phys. Rep.* **339**, 79 (2000), URL [https://doi.org/10.1016/S0370-1573\(00\)00071-5](https://doi.org/10.1016/S0370-1573(00)00071-5).

[10] V. M. Shabaev and V. A. Yerokhin, *Phys. Rev. Lett.* **88**, 091801 (2002), URL <https://doi.org/10.1103/PhysRevLett.88.091801>.

[11] V. A. Yerokhin, P. Indelicato, and V. M. Shabaev, *Phys. Rev. Lett.* **89**, 143001 (2002), URL <https://doi.org/10.1103/PhysRevLett.89.143001>.

[12] K. Pachucki, U. D. Jentschura, and V. A. Yerokhin, *Phys. Rev. Lett.* **93**, 150401 (2004), [erratum: *ibid.*, **94**, 229902 (2005)], URL <https://doi.org/10.1103/PhysRevLett.93.150401>.

[13] K. Pachucki, A. Czarnecki, U. D. Jentschura, and V. A. Yerokhin, *Phys. Rev. A* **72**, 022108 (2005), URL <https://doi.org/10.1103/PhysRevA.72.022108>.

[14] A. Czarnecki and R. Szafron, *Phys. Rev. A* **94**, 060501 (2016), URL <https://link.aps.org/doi/10.1103/PhysRevA.94.060501>.

[15] A. Czarnecki, M. Dowling, J. Piclum, and R. Szafron, *Phys. Rev. Lett.* **120**, 043203 (2018), URL <https://link.aps.org/doi/10.1103/PhysRevLett.120.043203>.

[16] A. Czarnecki, J. Piclum, and R. Szafron, *Phys. Rev. A* **102**, 050801(R) (2020), URL <https://link.aps.org/doi/10.1103/PhysRevA.102.050801>.

[17] V. A. Yerokhin and Z. Harman, *Phys. Rev. A* **88**, 042502 (2013), URL <https://link.aps.org/doi/10.1103/PhysRevA.88.042502>.

[18] V. Debierre, B. Sikora, H. Cakir, N. S. Oreshkina, V. A. Yerokhin, C. H. Keitel, and Z. Harman, *Phys. Rev. A* **103**, L030802 (2021), URL <https://link.aps.org/doi/10.1103/PhysRevA.103.L030802>.

[19] V. A. Yerokhin, P. Indelicato, and V. M. Shabaev, *Phys. Rev. Lett.* **91**, 073001 (2003), URL <https://doi.org/10.1103/PhysRevLett.91.073001>.

[20] V. A. Yerokhin, P. Indelicato, and V. M. Shabaev, *Phys. Rev. A* **71**, 040101(R) (2005), URL <https://doi.org/10.1103/PhysRevA.71.040101>.

[21] V. A. Yerokhin, P. Indelicato, and V. M. Shabaev, *Phys. Rev. Lett.* **97**, 253004 (2006), URL <https://doi.org/10.1103/PhysRevLett.97.253004>.

[22] V. A. Yerokhin, *Phys. Rev. A* **80**, 040501(R) (2009), URL <https://doi.org/10.1103/PhysRevA.80.040501>.

[23] V. A. Yerokhin, *Phys. Rev. A* **97**, 052509 (2018), URL <https://link.aps.org/doi/10.1103/PhysRevA.97.052509>.

[24] V. A. Yerokhin, Z. Harman, and C. H. Keitel, *Phys. Rev. Lett.* **133**, 251803 (2024), URL <https://link.aps.org/doi/10.1103/PhysRevLett.133.251803>.

[25] V. A. Yerokhin, Z. Harman, and C. H. Keitel, *Phys. Rev. A* **111**, 042820 (2025), URL <https://link.aps.org/doi/10.1103/PhysRevA.111.042820>.

[26] B. Sikora, Ph.D. thesis, Ruperto-Carola-University of Heidelberg (2018), URL <http://dx.doi.org/10.11588/heidok.00024575>.

[27] B. Sikora, V. A. Yerokhin, N. S. Oreshkina, H. Cakir, C. H. Keitel, and Z. Harman, *Phys. Rev. Research* **2**, 012002 (2020), URL <https://link.aps.org/doi/10.1103/PhysRevResearch.2.012002>.

[28] B. Sikora, V. A. Yerokhin, C. H. Keitel, and Z. Harman, *Phys. Rev. Lett.* **134**, 123001 (2025), URL <https://link.aps.org/doi/10.1103/PhysRevLett.134.123001>.

[29] V. A. Yerokhin and V. M. Shabaev, *Phys. Rev. A* **64**, 062507 (2001), URL <https://doi.org/10.1103/PhysRevA.64.062507>.

[30] V. A. Yerokhin, P. Indelicato, and V. M. Shabaev, *Eur. Phys. J. D* **25**, 203 (2003), URL <https://doi.org/10.1140/epjd/e2003-00270-x>.

[31] V. A. Yerokhin, *Eur. Phys. J. D* **58**, 57 (2010).

[32] V. A. Yerokhin and U. D. Jentschura, *Phys. Rev. A* **81**, 012502 (2010), URL <https://doi.org/10.1103/PhysRevA.81.012502>.

[33] S. Mallampalli and J. Sapirstein, *Phys. Rev. A* **57**, 1548 (1998), URL <https://doi.org/10.1103/PhysRevA.57.1548>.

[34] V. A. Yerokhin and V. M. Shabaev, *Phys. Rev. A* **60**, 800 (1999), URL <https://doi.org/10.1103/PhysRevA.60.800>.

[35] V. A. Yerokhin and A. V. Maiorova, *Symmetry* **12**, 800 (2020), URL <https://doi.org/10.3390/sym12050800>.

[36] V. A. Yerokhin, P. Indelicato, and V. M. Shabaev, *Phys. Rev. A* **69**, 052503 (2004), URL <https://doi.org/10.1103/PhysRevA.69.052503>.

[37] S. A. Blundell, K. T. Cheng, and J. Sapirstein, *Phys. Rev. A* **55**, 1857 (1997), URL <https://doi.org/10.1103/PhysRevA.55.1857>.

[38] V. A. Yerokhin, A. N. Artemyev, T. Beier, G. Plunien, V. M. Shabaev, and G. Soff, *Phys. Rev. A* **60**, 3522 (1999), URL <https://doi.org/10.1103/PhysRevA.60.3522>.

[39] V. A. Yerokhin, K. Pachucki, and V. M. Shabaev, *Phys. Rev. A* **72**, 042502 (2005), URL <https://doi.org/10.1103/PhysRevA.72.042502>.

[40] I. Angeli and K. Marinova, *At. Dat. Nucl. Dat. Tabl.* **99**, 69 (2013), URL <http://www.sciencedirect.com/science/article/pii/S0092640X12000265>.

[41] B. Ohayon, *Atomic Data and Nuclear Data Tables* **165**, 101732 (2025), URL <https://www.sciencedirect.com/>

science/article/pii/S0092640X25000257.

[42] S. Sturm, I. Arapoglou, A. Egl, M. Höcker, S. Kraemer, T. Sailer, B. Tu, A. Weigel, R. Wolf, J. C. López-Urrutia, et al., The European Physical Journal Special Topics **227**, 1425 (2019), URL <https://link.springer.com/content/pdf/10.1140/epjst/e2018-800225-2.pdf>.

[43] J. Sapirstein and K. T. Cheng, Phys. Rev. A **108**, 042804 (2023), URL <https://link.aps.org/doi/10.1103/PhysRevA.108.042804>.

[44] V. A. Yerokhin, Z. Harman, and C. H. Keitel, Phys. Rev. A **111**, 012802 (2025), URL <https://link.aps.org/doi/10.1103/PhysRevA.111.012802>.

[45] V. A. Yerokhin, K. Pachucki, M. Puchalski, C. H. Keitel, and Z. Harman, Phys. Rev. A **102**, 022815 (2020), URL <https://link.aps.org/doi/10.1103/PhysRevA.102.022815>.

Appendix A: Zeeman vertex function in momentum space

The angular integrations in the Zeeman vertex function are performed in momentum space as explained in Ref. [32]. The result is expressed as (*cf.* Eq. (30) of Ref. [32])

$$\begin{aligned} \langle n_1 \kappa_1 \mu_1 | \gamma^0 \Lambda_{\text{Zee}}(\varepsilon_1, \varepsilon_2) | n_2 \kappa_2 \mu_2 \rangle = A_\rho \frac{\alpha}{48\pi^5} \int_0^\infty dp_1 dp_2 \int_{|p_1-p_2|}^{p_1+p_2} dq p_1 p_2 q e^{-q^2/\rho^2} (-1)^{(l_1-l_2)/2} \\ \times \left\{ \left[-p_1 K_1(\kappa_1, \mu_1; \kappa_2, \mu_2) + p_2 K'_1(\kappa_1, \mu_1; \kappa_2, \mu_2) \right] \mathcal{R}_1(p_1, p_2, q) \right. \\ + \left[-p_1 K_1(-\kappa_1, \mu_1; -\kappa_2, \mu_2) + p_2 K'_1(-\kappa_1, \mu_1; -\kappa_2, \mu_2) \right] \mathcal{R}_2(p_1, p_2, q) \\ - p_1 p_2 K_2(\kappa_1, \mu_1; \kappa_2, \mu_2) [\mathcal{R}_3(p_1, p_2, q) + \mathcal{R}_4(p_1, p_2, q)] \\ \left. - p_1 p_2 K_2(-\kappa_1, \mu_1; -\kappa_2, \mu_2) [\mathcal{R}_5(p_1, p_2, q) + \mathcal{R}_6(p_1, p_2, q)] \right\}, \end{aligned} \quad (\text{A1})$$

where $\kappa_{1,2}$ and $\mu_{1,2}$ are the relativistic angular momentum quantum number and the angular-momentum projection of the states n_1 and n_2 , respectively, $\mathcal{R}_i(p_1, p_2, q)$ are the one-loop vertex functions given by Eqs. (A7)–(A12) of Ref. [38] and K_1 , K'_1 , and K_2 are basic angular integrals.

The angular integrals are defined as (*cf.* Eqs. (A7a)–(A7c) of Ref. [32])

$$\frac{3i}{4\pi} \int d\hat{p}_1 d\hat{p}_2 f(p_1, p_2, \xi) \chi_{\kappa_1 \mu_1}^\dagger(\hat{p}_1) [\hat{p}_1 \times \vec{\sigma}]_z \chi_{-\kappa_2 \mu_2}(\hat{p}_2) = \int_{-1}^1 d\xi f(p_1, p_2, \xi) K_1(\kappa_1, \mu_1; \kappa_2, \mu_2), \quad (\text{A2})$$

$$\frac{3i}{4\pi} \int d\hat{p}_1 d\hat{p}_2 f(p_1, p_2, \xi) \chi_{\kappa_1 \mu_1}^\dagger(\hat{p}_1) [\hat{p}_2 \times \vec{\sigma}]_z \chi_{-\kappa_2 \mu_2}(\hat{p}_2) = \int_{-1}^1 d\xi f(p_1, p_2, \xi) K'_1(\kappa_1, \mu_1; \kappa_2, \mu_2), \quad (\text{A3})$$

$$\frac{3i}{4\pi} \int d\hat{p}_1 d\hat{p}_2 f(p_1, p_2, \xi) \chi_{\kappa_1 \mu_1}^\dagger(\hat{p}_1) [\hat{p}_1 \times \hat{p}_2]_z \chi_{\kappa_2 \mu_2}(\hat{p}_2) = \int_{-1}^1 d\xi f(p_1, p_2, \xi) K_2(\kappa_1, \mu_1; \kappa_2, \mu_2), \quad (\text{A4})$$

where $\hat{p} = \vec{p}/|\vec{p}|$, $\xi = \hat{p}_1 \cdot \hat{p}_2$ and $f(p_1, p_2, \xi)$ is an arbitrary function.

The angular integrals K_1 and K'_1 are evaluated as

$$\left. \begin{aligned} K_1(\kappa_1, \mu_1; \kappa_2, \mu_2) \\ K'_1(\kappa_1, \mu_1; \kappa_2, \mu_2) \end{aligned} \right\} = \sqrt{\frac{3}{2}} (-1)^{j_1+\mu_1} C_{j_2 \mu_2, j_1 - \mu_1}^{10} S_{11}(\kappa_1, -\kappa_2) \times \left\{ \begin{aligned} P_{\bar{l}_2}(\xi) \\ P_{l_1}(\xi) \end{aligned} \right\}, \quad (\text{A5})$$

where $l_1 = |\kappa_1 + 1/2| - 1/2$, $\bar{l}_2 = |\kappa_2 - 1/2| - 1/2$, the angular coefficients $S_{JL}(\kappa_a, \kappa_b)$ are defined by Eqs. (C7)–(C9) of Ref. [38], $C_{j_1 m_1, j_2 m_2}^{jm}$ are the Clebsch-Gordan coefficients and $P_l(\xi)$ are the Legendre polynomials. For $\kappa_1 = \kappa_2$ and $\mu_1 = \mu_2 = 1/2$, the above formula reproduces the results of Eq. (A8a) of Ref. [38].

The angular integral K_2 is calculated to be

$$\begin{aligned} K_2(\kappa_1, \mu_1; \kappa_2, \mu_2) = 2\sqrt{2}\pi \sum_{L=L_{\min}}^{L_{\max}} P_L(\xi) \sum_{m=0, \pm 1} \sum_{\sigma=\pm 1/2} C_{1m, 1-m}^{10} C_{l_1 m_1, 1/2\sigma}^{j_1 \mu_1} C_{l_2 m_2, 1/2\sigma}^{j_2 \mu_2} \\ \times R_3(l_1, m_1, 1, m, L, M) R_3(L, M, 1, -m, l_2, m_2), \end{aligned} \quad (\text{A6})$$

where $L_{\min} = \max(0, l_1 - 1, l_2 - 1)$, $L_{\max} = \min(l_1 + 1, l_2 + 1)$, and

$$R_3(l_1, m_1, l_2, m_2, l_3, m_3) = \int d\hat{p} Y_{l_1 m_1}^*(\hat{p}) Y_{l_2 m_2}(\hat{p}) Y_{l_3 m_3}(\hat{p}). \quad (\text{A7})$$

For $\kappa_1 = \kappa_2$ and $\mu_1 = \mu_2 = 1/2$, the above formulas give the results of Eq. (A8c) of Ref. [38]. The dependence of K_2 on the projection of momenta is easily factorized as

$$K_2(\kappa_1, \mu_1; \kappa_2, \mu_2) = \frac{(-1)^{j_1-\mu_1} C_{j_2\mu_2, j_1-\mu_1}^{10}}{(-1)^{j_1-1/2} C_{j_2^{1/2}, j_1-1/2}^{10}} K_2(\kappa_1, 1/2; \kappa_2, 1/2), \quad (\text{A8})$$

so that it is sufficient to compute K_2 for $\mu_1 = \mu_2 = 1/2$ only.

As a test, we calculate the matrix element of the regularized magnetic potential $V_{g,\rho}$ in momentum space, which can be expressed in a similar way,

$$\begin{aligned} \langle n_1 \kappa_1 \mu_1 | V_{g,\rho} | n_2 \kappa_2 \mu_1 \rangle = & A_\rho \frac{\alpha}{12\pi^4} \int_0^\infty dp_1 dp_2 \int_{|p_1-p_2|}^{p_1+p_2} dq p_1 p_2 q e^{-q^2/\rho^2} (-1)^{(l_1-l_2)/2} \\ & \times \left\{ \left[-p_1 K_1(\kappa_1, \mu_1; \kappa_2, \mu_2) + p_2 K'_1(\kappa_1, \mu_1; \kappa_2, \mu_2) \right] g_{n_1 \kappa_1}(p_1) f_{n_2 \kappa_2}(p_2) \right. \\ & \left. + \left[-p_1 K_1(-\kappa_1, \mu_1; -\kappa_2, \mu_2) + p_2 K'_1(-\kappa_1, \mu_1; -\kappa_2, \mu_2) \right] f_{n_1 \kappa_1}(p_1) g_{n_2 \kappa_2}(p_2) \right\}, \end{aligned} \quad (\text{A9})$$

where $g_{n\kappa}(p)$ and $f_{n\kappa}(p)$ are the upper and the lower radial components of the Dirac wave function in momentum space, see Eq. (6) of Ref. [38].

Appendix B: Angular integration in the vertex overlapping contribution

For performing integrations over the angular variables in E_{OV}^P , it is convenient to switch to the spectral representation of the Green function. After angular integrations are carried out, the resulting formulas can be easily rewritten in terms of radial components of the Green function. Furthermore, it is sufficient to consider the unsubtracted (“unsub”) contribution, since the expressions for the subtraction term will be fully analogous. We thus write Eq. (71), omitting the subtraction part, as

$$\begin{aligned} E_{\text{OV}}^P(\text{unsub}) = & -4i\alpha \int_{C_F} d\omega \int \frac{d\vec{p}_1}{(2\pi)^3} \frac{d\vec{p}_2}{(2\pi)^3} \int d\vec{z} d\vec{y} \frac{e^{-i\vec{q}\cdot\vec{z}}}{\omega^2 - \vec{q}^2 + i0} \sum_{n_1 n_2} \frac{1}{(E - \varepsilon_{n_1})(E - \varepsilon_{n_2})} \psi_a^\dagger(\vec{z}) \alpha_\mu \psi_{n_1}(\vec{z}) \\ & \times \psi_{n_1}^\dagger(\vec{y}) V_g(\vec{y}) \psi_{n_2}(\vec{y}) \psi_{n_2}^\dagger(\vec{p}_1) \gamma^0 \Gamma_R^\mu(E, \vec{p}_1; \varepsilon_a, \vec{p}_2) \psi_a(\vec{p}_2). \end{aligned} \quad (\text{B1})$$

Following the procedure, described in Ref. [30] for the Lamb shift, we transform the above formula as follows

$$\begin{aligned} E_{\text{OV}}^P(\text{unsub}) = & -\frac{i\alpha^2}{2\pi^4} \int_{C_F} d\omega \int_0^\infty dp_1 dp_2 \int \frac{d\hat{\vec{p}}_1 d\hat{\vec{p}}_2}{8\pi^2} \frac{(p_1 p_2)^2}{\omega^2 - \vec{q}^2 + i0} \sum_{n_1 n_2} \frac{1}{(E - \varepsilon_{n_1})(E - \varepsilon_{n_2})} \\ & \times \left\{ \sum_J i^{l_2-l_a-J} C_J(\kappa_1, \kappa_a) R_J^{(1)}(q, an_1) P(n_1 n_2) \left[\mathcal{F}_1^{n_2 a} t_J(\kappa_1, \kappa_2, \kappa_a) + \mathcal{F}_2^{n_2 a} t_J(\kappa_1, -\kappa_2, -\kappa_a) \right] \right. \\ & - \sum_{JL} i^{l_2-l_a-L+1} R_{JL}^{(2)}(q, an_1) P(n_1 n_2) \left[\mathcal{R}_1^{n_2 a} s_{JL}^\sigma(\kappa_1, \kappa_2, -\kappa_a) + \mathcal{R}_2^{n_2 a} s_{JL}^\sigma(\kappa_1, -\kappa_2, \kappa_a) \right. \\ & \left. \left. + p_1 \mathcal{R}_3^{n_2 a} s_{JL}^{p_1}(\kappa_1, \kappa_2, \kappa_a) + p_2 \mathcal{R}_4^{n_2 a} s_{JL}^{p_2}(\kappa_1, \kappa_2, \kappa_a) + p_1 \mathcal{R}_5^{n_2 a} s_{JL}^{p_1}(\kappa_1, -\kappa_2, -\kappa_a) + p_2 \mathcal{R}_6^{n_2 a} s_{JL}^{p_2}(\kappa_1, -\kappa_2, -\kappa_a) \right] \right\}, \end{aligned} \quad (\text{B2})$$

where the functions $\mathcal{F}_i^{n_2 a}$ and $\mathcal{R}_i^{n_2 a}$ come from the vertex operator sandwiched between the Dirac wave functions (see Eqs. (147) and (148) of Ref. [30]) and the angular coefficients are defined by (cf. Eqs. (150) and (151) of Ref. [30])

$$t_J(\kappa_1, \kappa_2, \kappa_a) = \sum_{\mu_1 \mu_2 M} (-1)^{j_1-\mu_1} C_{j_2 \mu_2, j_1-\mu_1}^{10} s_{JM}^{n_1 a} \chi_{\kappa_2 \mu_2}^\dagger(\hat{\vec{p}}_1) Y_{JM}(\hat{\vec{q}}) \chi_{\kappa_a \mu_a}(\hat{\vec{p}}_2), \quad (\text{B3})$$

$$s_{JL}^\sigma(\kappa_1, \kappa_2, \kappa_a) = \sum_{\mu_1 \mu_2 M} (-1)^{j_1-\mu_1} C_{j_2 \mu_2, j_1-\mu_1}^{10} s_{JM}^{n_1 a} \chi_{\kappa_2 \mu_2}^\dagger(\hat{\vec{p}}_1) \vec{\sigma} \cdot \vec{Y}_{JLM}(\hat{\vec{q}}) \chi_{\kappa_a \mu_a}(\hat{\vec{p}}_2), \quad (\text{B4})$$

$$s_{JL}^{p_i}(\kappa_1, \kappa_2, \kappa_a) = \sum_{\mu_1 \mu_2 M} (-1)^{j_1-\mu_1} C_{j_2 \mu_2, j_1-\mu_1}^{10} s_{JM}^{n_1 a} \chi_{\kappa_2 \mu_2}^\dagger(\hat{\vec{p}}_1) \hat{\vec{p}}_i \cdot \vec{Y}_{JLM}(\hat{\vec{q}}) \chi_{\kappa_a \mu_a}(\hat{\vec{p}}_2). \quad (\text{B5})$$

Furthermore, the radial integrals are (cf. Eqs. (145) and (146) of Ref. [30])

$$R_J^{(1)}(q, an) = C_J(\kappa_n, \kappa_a) \int_0^\infty dx x^2 j_J(qx) (g_a g_n + f_a f_n), \quad (\text{B6})$$

$$R_{JL}^{(2)}(q, an) = \int_0^\infty dx x^2 j_L(qx) \left[g_a f_n S_{JL}(\kappa_a, -\kappa_n) - f_a g_n S_{JL}(-\kappa_a, \kappa_n) \right], \quad (\text{B7})$$

$$P(n_1, n_2) = 2 \frac{-\kappa_1 - \kappa_2}{\sqrt{3}} C_1(-\kappa_2, \kappa_1) \int_0^\infty dx x^3 (g_{n_1} f_{n_2} + f_{n_1} g_{n_2}), \quad (\text{B8})$$

where $q = |\vec{q}|$, $g_a = g_a(x)$ and $f_a = f_a(x)$ are components of radial wave functions, and $j_l(z)$ is the spherical Bessel function. The standard angular coefficients $C_L(\kappa_1, \kappa_2)$ and $S_{JL}(\kappa_1, \kappa_2)$ can be found, e.g., in Appendix C of Ref. [30].

Now we turn to the integration over $\hat{\vec{p}}_1$ and $\hat{\vec{p}}_2$ in Eq. (B2). It is complicated by the fact that we have to integrate out all angles except for $\xi = \hat{\vec{p}}_1 \cdot \hat{\vec{p}}_2$ analytically, whereas the remaining integration over ξ can be performed only numerically. We perform angular integration with the help of the following identity (see Appendix C of Ref. [45])

$$\frac{1}{8\pi^2} \int d\hat{\vec{p}}_1 d\hat{\vec{p}}_2 f(q) G(\hat{\vec{p}}_1, \hat{\vec{p}}_2) = \int_{-1}^1 d\xi f(q) \hat{G}(\xi), \quad (\text{B9})$$

where $f(q)$ and $G(\hat{\vec{p}}_1, \hat{\vec{p}}_2)$ are arbitrary functions of the specified arguments and

$$\hat{G}(\xi) = \frac{1}{4\pi} \sum_{lm} P_l(\xi) \int d\hat{\vec{p}}_1 d\hat{\vec{p}}_2 Y_{lm}(\hat{\vec{p}}_1) Y_{lm}^*(\hat{\vec{p}}_2) G(\hat{\vec{p}}_1, \hat{\vec{p}}_2). \quad (\text{B10})$$

With help of Eqs. (B9) and (B10) we can integrate out all angles except ξ in the angular coefficients t_J , s_{JL}^σ , $s_{JL}^{P_{1,2}}$, in a similar way to that described in Eqs. (C14)-(C20) of Ref. [45]. The calculation is quite straightforward but tedious; the resulting formulas are too long to be presented here explicitly. What is unfortunate, however, is not the length of the formulas, but their numerical instability in the region $q \rightarrow 0$ and for large J . Because of this we had to employ the extended-precision arithmetic (up to 64 decimal digits) for computation of these angular coefficients. Even so, we were able to extend the partial-wave expansion in E_{OV}^P only up to $|\kappa_{\text{max}}| = 15$, since for higher partial waves even the 64-digit arithmetic was not sufficient. This situation contrasts with the case of the Lamb shift, where a numerically stable algorithm for computing the analogous angular factors was found, as described in Appendix C of Ref. [31]. Unfortunately, we have not been able to extend this stable algorithm to the g -factor case.